The Astrophysical Journal, 999:234 (18pp), 2026 March 10 https://doi.org/10.3847/1538-4357/ae3d9e

Type Iax Supernovae as a Source of Iron-rich Silicate Dust

Aman Kumar[1,2] and Arkaprabha Sarangi[1]
[1] Indian Institute of Astrophysics, 100 Feet Rd, Koramangala, Bengaluru, Karnataka 560034, India
[2] Academy of Scientific and Innovative Research (AcSIR), Ghaziabad, Uttar Pradesh 201002, India
Received 2025 November 18; revised 2026 January 15; accepted 2026 January 22; published 2026 March 6

Abstract

We model the formation of dust in the ejecta of Type Iax supernovae (SNe), which is a low-luminosity subclass of Type Ia SNe. A nonequilibrium chemical kinetic approach is adopted to trace the synthesis of molecules, molecular clusters, and dust grains in the ejecta of thermonuclear SNe. We find that Type Iax SNe provide conditions conducive to the formation of several O-rich dust species in the ejecta. Particularly, iron-rich silicates of chemical types ($FeSiO_3$), (Fe_2SiO_4), and ($MgFeSiO_4$) are found to form in abundance, suggesting that the ejecta of low-luminosity thermonuclear SNe can be a site where a large fraction of iron is locked up in dust, unlike other stellar sources. The final mass of dust formed in the ejecta ranges between 10^{-5} and 10^{-4} $M_{\odot}$, where most of the dust forms between 1000 and 2000 day postexplosion. Apart from Fe-rich silicates, Mg-silicates and silicon carbide are also formed in the ejecta of Type Iax SNe. When compared to the dust budget of typical Type Ia SNe, we find that the expected dust-to-ejecta mass ratio is 1 or 2 orders of magnitude larger in Type Iax SNe. We conclude that the ejecta of typical Type Ia SNe form a negligible amount of dust, in agreement with observations, while the low-luminosity subclass Type Iax SNe are potential producers of iron-rich silicates.

Unified Astronomy Thesaurus concepts: Type Ia supernovae (1728); Dust formation (2269); Astrochemistry (75); Circumstellar dust (236)

1. Background

Thermonuclear supernovae (SNe) have a white dwarf (WD) progenitor in a binary system, but they have a number of explosion channels, giving us a wide variety of peculiar SNe (F. Hoyle & W. A. Fowler 1960; Z.-W. Liu et al. 2023). A Type Iax SN is a subclass of Type Ia thermonuclear SN, earlier termed as "peculiar Ia," that is fainter and less energetic than the more common Type Ia. SN 2002cx was the first peculiar Type Ia SN observed by W. Li et al. (2003) and R. J. Foley et al. (2013), so they are also termed as "02cx-like." Unlike their Type Ia cousins, Type Iax SNe do not entirely destroy the WD during the explosion, instead leaving behind a stellar remnant. They are also termed as failed SNe, which leave behind a "zombie" star (R. J. Foley et al. 2014; M. Kawabata et al. 2018, 2021). This bound remnant might be affecting the light curve (R. J. Foley et al. 2016; M. R. Magee et al. 2016). They are characterized by their lower-luminosity, lower ejecta velocities, and a lack of a secondary maximum in their near-infrared light curves (D. Kasen 2006; M. R. Magee et al. 2025). The classification is based on observational properties, including their unique spectral features of a prominent Fe III line and weak Si II and S II lines (D. Branch et al. 2004) and light curves that are fainter and evolve more slowly than typical Type Ia SNe (R. J. Foley et al. 2013). Even among Type Iax, there is a wide range in the peak absolute brightness ($M_v = -14$ to -18 mag) (R. J. Foley et al. 2013; M. Singh et al. 2018; L. A. Kwok et al. 2025; M. Singh et al. 2025).

W. Li et al. (2001) and R. J. Foley et al. (2013) estimate that Type Iax SNe have a 30% occurrence rate as compared to Type Ia in a selected sample space, which is further constrained to ∼5% by G. Dimitriadis et al. (2025) using Zwicky Transient Facility SN Ia Data. There are around 5–10 Type Iax SNe classified detections per year. Type Iax SNe are estimated to originate from a single degenerate channel. In a Type Ia single degenerate channel explosion, a deflagration subsonic wave originates within the WD core, which preexpands in the WD, and spontaneously, the subsonic wave converts into a supersonic wave and explodes (S. E. Woosley et al. 1986; P. Hoeflich et al. 1995; F. K. Röpke & J. C. Niemeyer 2007; F. K. Röpke et al. 2007; I. R. Seitenzahl et al. 2013). This is known as the delayed-detonation (DDT) model, the detonation burns down the WD constituents to ^{56}Ni, and the preexpansion due to the deflagration wave quenches the burning, so that we are left with some intermediate-mass elements (IMEs) and iron-group elements (IGEs) like Si and Mg. This model resembles the observed abundances and high ^{56}Ni content of Type Ia SN ejecta. In Type Iax SNe, the lower ejecta velocity, low ^{56}Ni content, and no secondary maximum in the infrared light curve, which suggests well-mixed ejecta, can be explained by a pure deflagration model (V. N. Gamezo et al. 2003; D. García-Senz & E. Bravo 2005; F. K. Röpke et al. 2006; G. C. Jordan et al. 2012; H. Ma et al. 2013; M. Fink et al. 2014; M. Long et al. 2014; Z.-W. Liu et al. 2015; B. Barna et al. 2018; M. Zhang et al. 2019; F. Lach et al. 2022; L. A. Kwok et al. 2025). In the pure deflagration model, the subsonic deflagration wave never goes into the supersonic phase, and depending upon its energy, it ejects some of the outer parts of the WD, which also explains the wide range in peak absolute brightness of Type Iax SN. Deflagration quenches the nuclear burning of C/O WD, which leaves us with less ^{56}Ni content with well-mixed high abundances of C, O, and other IME like Mg, Si, and S. The centrally peaked emission lines detected by JWST in early nebular spectra of Type Iax SN 2024pxl and SN 2024vjm also indicate the mixing of metals among all the radial layers (L. A. Kwok et al. 2025).

Cosmic dust is made of clusters of different sizes of diverse chemical nature. Dust formation requires moderately high

temperatures, in the range of 1000–2000 K, and high gas density with abundances of the refractory elements (A. Sarangi et al. 2018). Core-collapse SNe, outflows from Asymptotic Giant Branch (AGB) stars, mass ejections from luminous blue variables, and Wolf–Rayet stars are responsible for the dust formations (E. Dwek & I. Cherchneff 2011). SNe are one of the primary dust factories in galaxies. The ejecta of a core-collapse SN provide the necessary environmental conditions and chemical compositions for dust production. Especially Type II SNe, with a massive, slow-moving ejecta, are observationally confirmed to produce large masses of dust (M. Matsuura et al. 2015; G. C. Clayton et al. 2025; M. Shahbandeh et al. 2023).

Type Ia SN ejecta is dominated by ^{56}Ni, which will further decay into ^{56}Fe; they produce around 0.6 $M_{\odot}$ of ^{56}Ni (T. Nozawa et al. 2011). On the other side, core-collapse SNe have much smaller ^{56}Ni mass, around 0.055 $M_{\odot}$ (I. R. Seitenzahl et al. 2014; Ó. Rodríguez et al. 2023). Type Ia SNe, being highly energetic, do not show signs of dust formation (H. L. Gomez et al. 2012). Interestingly, Type Iax SNe being less energetic can be good candidates for dust production, and having significant ^{56}Ni, mixed microscopically in the entire ejecta, can provide a pathway for the synthesis of iron-rich dust.

Herschel PACS and SPIRE photometry at 70–500 μm of Type Ia remnants Tycho and Kepler find dust masses of $\sim 3 \times 10^{-3}\ M_{\odot}$ (H. L. Gomez et al. 2012), at a temperature of $\sim$ 82 K. The IR emission was found to be spatially consistent with the X-ray emitting region and the circumstellar region swept up by the SN blast wave. Very recently, a large mass of dust ($\sim 10^{-2}\ M_{\odot}$) was reported in Type Ia- circumstellar medium SN 2018evt, where the dust was estimated to form in the circumstellar environment (L. Wang et al. 2024). Evidence of new dust formation in the ejecta of Type Ia is yet to be confirmed by observations. Initial theoretical models have predicted new dust formation in the ejecta of Type Ia SNe, with significant dust masses, ranging between 10^{-4} and 0.1 $M_{\odot}$ (T. Nozawa et al. 2011). However, the approach adopted in those models may oversimplify the chemical evolution of the ejecta (B. Donn & J. A. Nuth 1985).

Spitzer observations found strong mid-IR emission in nearby (19 Mpc) Type Iax SN 2014dt, in 3.6 and 4.5 μm fluxes (O. D. Fox et al. 2016). A dust mass of about $10^{-5}\ M_{\odot}$ at $\sim$ 700 K was estimated by a single carbon dust component fit (O. D. Fox et al. 2016). The SN remnant 1181 was estimated to have the origin in Type Iax SN Pa 30, which shows dust emission in the far-IR through IRAS and AKARI imaging (F. Lykou et al. 2023; T. Cunningham et al. 2024); however, it is difficult to distinguish between dust produced in the ejecta and in the swept-up interstellar matter (ISM)/circumstellar matter. Interestingly, based on the X-ray properties, the SN remnant Sagittarius A East in our Galactic center is reported to be of Type Iax origin, and also hosts large masses of warm dust (0.02 $M_{\odot}$) (P. Zhou et al. 2021). Even though all the dust may not have condensed in the ejecta alone, it projects a strong case for Type Iax SNe to be dust producers in galaxies. In this paper, we will explore the possibility of dust production in Type Iax SNe and also compare our results with Type Ia SNe.

2. Rationale of This Work

SN Type Iax is a subclass of thermonuclear SN explosions. Similar to Type Ia, they are rich in IME and IGE (L. Li et al. 2018). Also, the light curve of Type Iax SNe is powered by γ-rays produced by radioactive decay of ^{56}Ni→^{56}Co→^{56}Fe (S. A. Colgate & C. McKee 1969; W. D. Arnett 1982; W. Hillebrandt et al. 2013; B. Barna et al. 2018). Unlike typical Type Ia explosions, which are energetic, fast expanding (10,000–20,000 km s^{-1}) (S. Srivastav et al. 2023), have secondary maximum in their near-infrared light curves (J. Elias et al. 1981), and completely disrupt the progenitor WD (M. C. Bersten & P. A. Mazzali 2017; Z.-W. Liu et al. 2023), Type Iax explosions are less energetic, exhibit lower ejecta velocities (2000–7000 km s^{-1}) (S. W. Jha 2017; S. W. Jha et al. 2019), and may leave behind a bound remnant (R. J. Foley et al. 2014). These factors lead to slower expansion and higher ejecta densities at a time when the temperature is lower than the ionization temperature, allowing atoms and molecules to collide more frequently and enhancing dust nucleation rates. The presence of significant unburned carbon and oxygen is expected to form the necessary dust-precursor molecules in the chemically mixed ejecta, providing the important ingredients for the formation of iron-rich dust species.

The paper progresses from the physical properties of Type Iax ejecta to the formation of dust and its astrophysical context. The following Section 3 introduces the ejecta properties of Type Iax SNe, beginning with a review of explosion models and progenitor channels from the literature, and summarizing the key input parameters such as abundance profiles, temperature, densities of the system at 100 days after the explosion, along with their ^{56}Ni yield. Section 4 focuses on the chemistry of the ejecta, describing the reaction network, modifications implemented in this study, the species considered, and the reactions that are found to be the most important for dust formation. Section 5 addresses molecule formation, identifying key molecules produced in the ejecta and their relation to the dust species. Section 6 presents the dust budget, detailing dust types, quantities, and formation timescales. Section 7 describes the dust formation scenario in Type Ia and presents its dust mass evolution. Section 8 provides a broader discussion, including the "missing iron in the ISM" problem (C. Pinto et al. 2013; E. Dwek 2016; I. Psaradaki et al. 2023), the sensitivity of results to key parameters, and the need for further observational constraints. Finally, Section 9 summarizes the main findings and highlights their significance for understanding dust production in thermonuclear explosions.

3. Ejecta of Type Iax and Ia SNe

In this work, we adopt the three-dimensional pure deflagration model of M. Fink et al. (2014) as the mechanism for Type Iax SN explosion. We use I. R. Seitenzahl et al. (2013) DDT models for Type Ia SNe, which explore a wide range of ignition configurations within Chandrasekhar mass C/O WDs.

3.1. Various Progenitor Channels

M. Fink et al. (2014) models consider different numbers and geometries of ignition kernels, leading to variations in explosion strength, ejecta mass, and the mass of synthesized ^{56}Ni mentioned in Table 1. The ignition kernels are the origin site of the deflagration wave. The lower-kernel configurations (`N1def,N3def,N5def`) produce weaker explosions, with smaller ^{56}Ni masses and more massive bound remnants. The light curves predicted by several of these models and model densities show good agreement with those observed for certain

Table 1
The Deflagration Models Used in This Study, Mass of Ejecta (M_{ej}), Bound Remnant Mass (M_b), Synthesized ^{56}Ni Mass ($M_{^{56}Ni}$), Are in $M_\odot$, and Ejecta Kinetic Energy ($E_{kin,ej}$) Is in 10^{50} erg Unit; These Are from M. Fink et al. (2014)

Model	M_{ej}	M_b	$M_{^{56}Ni}$	$E_{kin,ej}$	SN	References
N1def	0.0843	1.32	0.0345	0.149	SN 2019muj, SN 2014dt SN 2024pxl	(B. Barna et al. 2021), (Y. Camacho-Neves et al. 2023) (L. A. Kwok et al. 2025)
N3def	0.195	1.21	0.073	0.439	SN 2002cx, SN 2015H	(B. Barna et al. 2018),
N5def	0.372	1.03	0.158	1.35	SN 2020udy SN 2005hk SN 2020rea	(K. Maguire et al. 2023) (B. Barna et al. 2018) (M. Singh et al. 2022)
N10def	0.478	0.926	0.183	1.95	SN 2011ay SN 2012Z	(B. Barna et al. 2018)
N20def	0.859	0.545	0.264	3.75	⋯	⋯
N40def	1.21	0.19	0.335	5.22	⋯	⋯
N100def	1.31	0.090	0.355	6.11	⋯	⋯

Note. The early light curves and densities of a few Type Iax SNe match these models in the mentioned references.

known Type Iax SNe SN 2014dt (Y. Camacho-Neves et al. 2023), SN 2019muj (B. Barna et al. 2021), SN 2005hk SN 2002cx, SN 2015H, SN 2011ay, SN 2012Z (B. Barna et al. 2018), SN 2020udy (K. Maguire et al. 2023), and SN 2020rea (M. Singh et al. 2022). The energetics and abundances from these models serve as our initial conditions, allowing us to investigate how differences in ignition channels influence the chemical composition and physical conditions relevant for molecule and dust formation. Higher configuration models (N150def, N200def, N300def, N1600def) are also available; however, they do not align with any of the current Type Iax observations, and therefore are not significant for our study.

I. R. Seitenzahl et al. (2013) uses a similar type of ignition kernel geometries for DDT models. The lower-kernel configurations (N1ddt, N3ddt, N5ddt) have fewer deflagration wave origin sites, which leads to less mixing. Following detonation, this results in more ^{56}Ni masses, while other elements are only present in the outer regions. The higher configuration models (N20ddt, N40ddt, N100ddt) have more deflagration ignition kernels, which will give well-mixed elemental composition up to the more inner regions, giving less ^{56}Ni abundance. N100ddt model among other models produces 0.6 $M_\odot$ of ^{56}Ni, which is similar to the estimated Type Ia ^{56}Ni content from observations (M. Stritzinger et al. 2006).

3.2. Abundances

Figure 1 shows the abundance profiles as a function of enclosed mass for a set of deflagration (N1def to N100def) models representing Type Iax SNe and DDT (N1ddt to N100ddt) models representing Type Ia SNe. The source data of I. R. Seitenzahl et al. (2013) and M. Fink et al. (2014)[3] provide abundances in radial coordinates at 100 s postexplosion. We derive the abundance distribution as a function of mass coordinates by integrating over the density profile (Figure 2).

The ejecta is characterized by a chemically mixed composition in the pure deflagration models. While ^{56}Ni is the most abundant species, the ejecta also contains significant amounts of O, C, and Si. The large abundance of unburnt C/O exceeds the mass of the Si/S, which is a consequence of the subsonic and turbulent nature of the deflagration flame, allowing the WD to expand and quench the burning before completion. This turbulent process thoroughly mixes the burned and unburned material.

In contrast, in the DDT models, the ejecta is more dominated by ^{56}Ni, with contributions from S, Si, and O. The explosion begins similarly to a Type Iax, with a subsonic deflagration flame that preexpands the entire WD, reducing its overall density. At some point, this deflagration spontaneously transitions into a detonation. A detonation is a supersonic shockwave that rips through the preexpanded star at immense speed. The highest-density material at the center burns to iron elements, while the lower-density material farther out burns to intermediate elements, creating a structure where elements are less mixed with a core of Ni/Fe and outer layers of Si/S. The powerful detonation is efficient at converting large portions of the WD's C/O into Si/S in intermediate-density layers. The dominating ^{56}Ni in both cases will eventually decay into ^{56}Co and then into ^{56}Fe, emitting highly energetic γ-rays. Large Fe abundances along the entire ejecta help to form iron-rich dust.

3.3. Gas Temperature

T. Nozawa et al. (2011) obtained temperature distributions for Type Ia gas ejecta using the deflagration models of K. Nomoto et al. (1984) and F.-K. Thielemann et al. (1986) for 100 and 300 days after the explosion. These temperature profiles follow a power law with the exponent −0.89 with time. For all DDT models, the ejecta mass is similar, and we scaled the normalized mass in Figure 3 to 1.4 $M_\odot$ ejecta mass. There is no model available for the temperature profile of Type Iax SN ejecta. We expect that, due to lower velocities and a bound remnant, the initial temperatures of Type Iax ejecta should be higher than those of Type Ia SN. D. Bánhidi et al. (2025) reported a photospheric temperature of 4475 K for SN 2022xlp at 90 days, M. Singh et al. (2022) reported 5500 K for SN 2020udy at 100–125 days, and ∼4500 K for SN 2020rea at 140 days. Additionally, M. Kawabata et al. (2018) reported a

[3] HESMA Hydro models: https://hesma.h-its.org/hydro/.

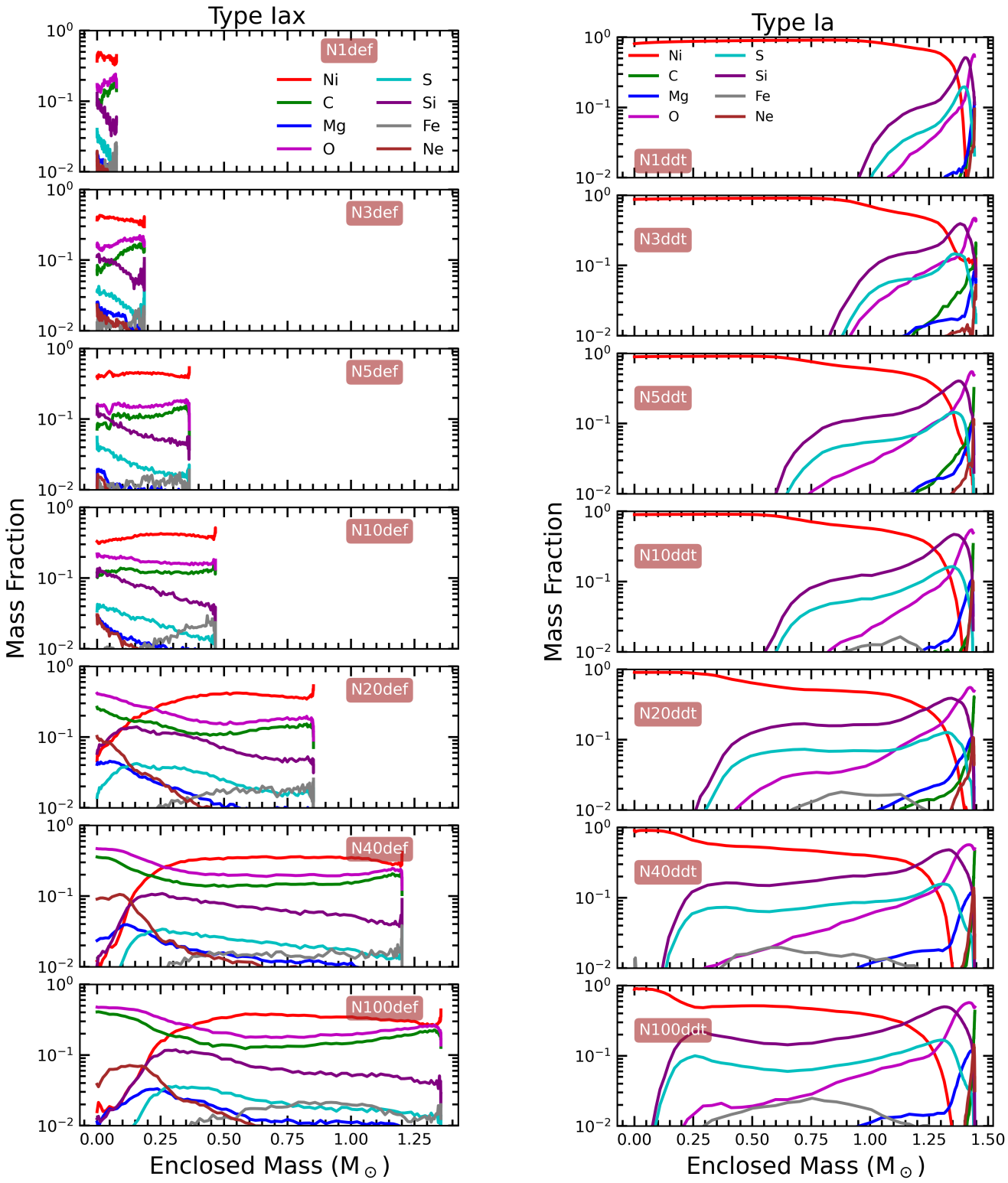

Figure 1. Left: abundance profile of deflagration models (Type Iax) in enclosed mass coordinate (M. Fink et al. 2014). Right: abundance profile of delayed-detonation models (Type Ia) in enclosed mass coordinate (I. R. Seitenzahl et al. 2013). Both models use a similar 1.4 $M_{\odot}$ initial mass of WD. Type Iax ejecta is increasing in mass for higher configuration models due to more powerful deflagration waves. Type Ia ejecta; as initial deflagration ignition sites are increasing, the ejecta is giving elements other than ^{56}Ni up to more inner regions.

photospheric temperature around 3700 K for Type Iax SN 2014dt at 132 days, and it remained constant until 410 days, after the explosion. However, at relatively early epochs (∼100 days), the ejecta of Type Iax SNe are expected to be optically thin due to their low ejecta masses (L. A. Kwok et al. 2025), so the gas temperature is expected to drop. Hence, the evolution of photospheric temperature should not be a tracer for the evolution of gas temperatures. In our study for Type Iax

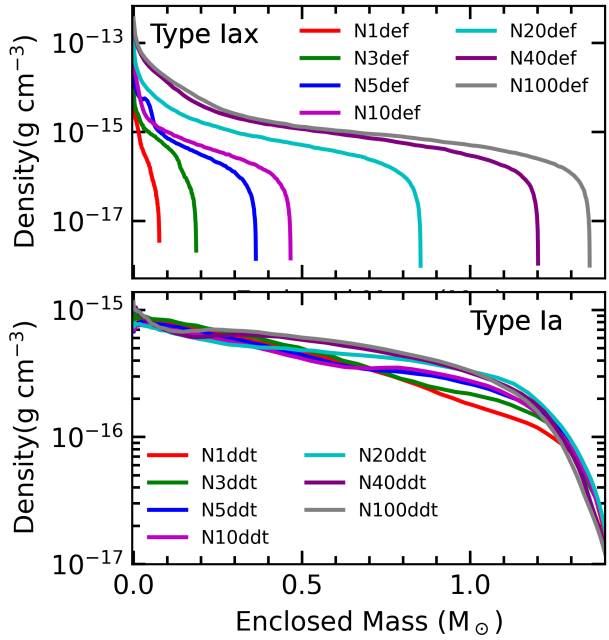

Figure 2. Top: density profile of M. Fink et al. (2014) deflagration models of Type Iax in enclosed mass coordinate at 100 days. Bottom: density profile of I. R. Seitenzahl et al. (2013) DDT models of Type Ia in enclosed mass coordinate at 100 days.

SN ejecta, we used the theoretical radial temperature profiles of Type Ia from D. Jack et al. (2011) at 50 days (shown in Figure 3) and scale according to the ejecta mass. Similar to Type Ia, we assume the temporal profiles to follow a power-law exponent of −0.89. Our model temperature for the inner ejecta at 100 days is comparable to the estimated photospheric temperature for SN 2014dt by M. Kawabata et al. (2018).

3.4. Gas Density

We use densities provided by M. Fink et al. (2014) at 100 s postexplosion, in velocity space. Figure 2 presents the density profiles as a function of enclosed mass, for deflagration and DDT models at 100 days. All deflagration models exhibit a steep density drop in the innermost regions, followed by a more gradual decline toward the outer layers. Lower-energy explosions (e.g., `N1def, N3def, N5def`) produce a small amount of ejecta with a sharp decline in the outer regions, while higher-energy models (e.g., `N40def, N100def`) display more extended density gradients.

The DDT models of I. R. Seitenzahl et al. (2013) have lower densities since the star was preexpanded and exploded by detonation. All models have similar densities, with slight differences in intermediate regions due to variations in the initial deflagration wave configurations.

4. Ejecta Chemistry

The chemical evolution of the SN ejecta is a complex interplay of various physical and chemical processes. We describe our chemical kinetic model, building upon previous work (A. Sarangi & I. Cherchneff 2013; A. Sarangi 2022) while incorporating new species and reactions relevant to the unique conditions of Type Iax SNe.

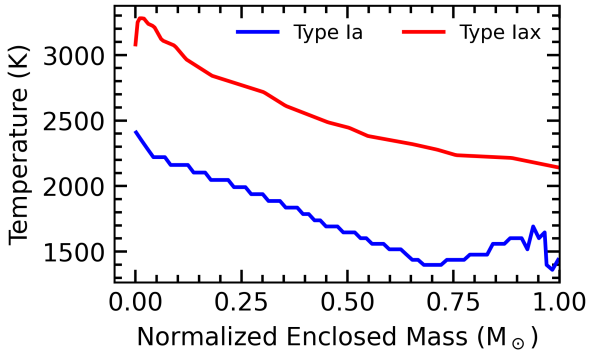

Figure 3. The Temperature profiles at 100 days used in this study. Type Ia temperature profile is taken from T. Nozawa et al. (2011), and the hotter profile of Type Iax is taken from D. Jack et al. (2011). The enclosed mass is normalized to the ejecta mass of the SN Ia ($M_{\rm ejecta}$ = 1.38 $M_\odot$) used in T. Nozawa et al. (2011). Both temperature profiles follow a power law with exponent −0.89 with time.

Our model is based on the well-established nonequilibrium chemistry solver algorithm (NECSA), which has been successfully applied to study the chemistry of Type II SN ejecta (A. Sarangi & I. Cherchneff 2013, 2015; A. Sarangi et al. 2018; A. Sarangi 2022). The formation of dust and molecules is based on simultaneous phases of nucleation and condensation (I. Cherchneff & E. Dwek 2009, 2010; A. Sarangi & I. Cherchneff 2015). The chemical network accounting for all possible reactions involving atoms, molecules, and molecular clusters present in the gas is modeled by A. Sarangi & I. Cherchneff (2013). A comprehensive list of chemical reactions is presented in I. Cherchneff & E. Dwek (2009) and A. Sarangi & I. Cherchneff (2013), encompassing both thermal and nonthermal processes. In this paper, we have significantly expanded the chemical network to account for a more comprehensive set of reactions involving iron and its compounds. We have added new species, including iron oxides, Mg–Fe silicates (pyroxenes and olivines); Table A1 lists all the new reactions. The nucleation proceeds by consecutive phases of Mg/Fe addition and oxidation by single O addition, O_2 and SO. Due to the lack of documentation, some of the rates are estimated using similar reactions with known reaction rates. Our final chemical network consists of 109 species and 504 reactions. It includes possible thermal and nonthermal processes constrained by the temperature and density conditions.

Nonthermal processes are mostly influenced by radioactive ^{56}Ni, which will further decay to ^{56}Co and then to ^{56}Fe , producing highly energetic γ-rays , which degrade to UV photons and Compton electrons (CE). They disrupt and delay the formation of both precursor molecules and dust grains. Type Iax SNe have a relatively smaller amount of ^{56}Ni as mentioned in Table 1, when compared to Type Ia SNe. The reactions with fast CE depend upon the amount of ^{56}Ni produced and the ejecta mass. For deflagration models `N1def, N10def, N100def`, the rates are given in Table A2 in Arrhenius form, calculated using the prescription of I. Cherchneff & E. Dwek (2009). However, Type Ia SN produces a significant amount of ^{56}Ni (around 0.6 $M_\odot$). Theoretical DDT models produce ^{56}Ni masses ranging from 1.11 to 0.6 $M_\odot$. Table A2 presents the CE rates for the `N100ddt` model with the lowest ^{56}Ni mass among all DDT models.

5. Molecules in the Ejecta of Type Iax Compared to Ia

We followed the evolution of the species from day 100 to 4100, postexplosion. The synthesis of diatomic molecules, namely, SiO, CO, O_2, SO, and SiS, is important in the ejecta in terms of their abundances and epochs of formation shown in Figure 4 (left panel for Type Iax and right panel for Type Ia). We begin our analysis of the ejecta chemistry from day 100 after the explosion. The conditions of the ejecta before that are not suitable for the synthesis of neutral molecules or clusters.

In Type Iax SNe, for all the models, CO abundance increases as early as 200 days and becomes almost saturated by 2000 days, postexplosion. There is no further change in the abundances of CO at late times since CO does not act as a precursor molecule to any dust species (A. Sarangi & I. Cherchneff 2013). SiO is the most important precursor molecule in dust production. The epoch of SiO depletion is similar to the epoch of the rise in dust masses, highlighting that the formation of SiO molecules in the ejecta leads to rapid conversion into small dust clusters. O_2 gets quickly depleted to form CO and SiO molecules, and continues to act as an oxidizing agent for O-rich clusters of silicates. The zones rich in Si and S and scarce in oxygen prefer the formation of SiS molecules. SO synthesized in the ejecta also has an oxidizing effect on the small clusters, similar to that of O_2. Despite large abundances of Fe atoms, the abundances of FeO molecules are not significant.

The ejecta of the DDT models (Type Ia SNe) are rich in Si, S, which explains the relatively much higher production of SiS than the CO molecules, and the production of SO molecules also increases in higher configuration models, which is missing in the deflagration models.

6. Dust Budget of Type Iax SNe

As discussed in Section 4, we introduced a chemical network (Table A1) for Fe–Mg silicates and iron oxides based on nucleation. For all of these models, there was no significant iron oxide production in the molecular phase. Pyroxenes like ferrosilite ($FeSiO_3$) and enstatite ($MgSiO_3$) are the most abundant dust species followed by olivines like fayalite (Fe_2SiO_4) and forsterite ($MgFeSiO_4$) species contributing to total dust mass, as shown in Figure 5. The formation of Fe-rich silicates is not proposed for Type II SNe (A. Sarangi & I. Cherchneff 2013), but the unique abundance distribution in Type Iax SNe leads to the formation of such silicates.

For Type Iax, the total ejecta in each model was divided into multiple zones of the same size, and then, the total dust mass was calculated by summing over all zones. Olivines like (Fe_2SiO_4) and ($MgFeSiO_4$) species form early in small masses at 300 days in the innermost zones. Later, at 1500 days, ($FeSiO_3$) and ($MgSiO_3$) appear in the innermost regions, leading to a sudden increase in dust masses. After this, we are still left with a lot of elements in free gas form, and free Si and C combine to form SiC at later times and become equally significant in higher configuration models.

The formation of different species and epochs of formation depends on the physical conditions of the environment and local chemistry. Figure 5 and Table 2 highlight the individual species contribution in each deflagration model of Type Iax SNe, along with a comparison between the dust production in different models. `N1def` and `N3def` models are low energy, have low ejecta mass, forming dust of masses around $3.7 \times 10^{-6}\ M_\odot$ and $1.2 \times 10^{-5}\ M_\odot$ at 4000 days after the explosion, respectively. `N20def`, `N40def`, and `N100def` are high-energy models with small bound remnant mass, have high ejecta mass giving a dust mass of $5.4 \times 10^{-5}\ M_\odot$ to $6.7 \times 10^{-5}\ M_\odot$ at 4000 days after the explosion. Intermediate models `N5def` and `N10def` produce dust masses of $2.8 \times 10^{-5}\ M_\odot$; however, the time of formation is earlier than the other cases.

All models vary in dust composition, depending on their ejecta mass, elemental composition, and ^{56}Ni content. Figure 6 (left panel) describes the dust formation zones as a function of time, in velocity space. As we see in the Figure 7, the dust-to-gas mass ratio of all the deflagration models is almost the same, i.e., 4–8 $\times 10^{-5}\ M_\odot$ at 4000 days (Table 3), suggesting that Type Iax SNe are efficient dust producers. Specifically, `N3def`, `N5def`, and `N10def` models provide the best conditions for dust production, and there are some observed SN candidates of these models as shown in Table 1.

6.1. Dust Masses in Type Iax SN 2012Z

The deflagration models we have used are theoretical simulations and can differ from the actual observational results. The early light curves of these models are comparable to some observed sources, as mentioned in Table 1. However, M. Singh et al. (2018, 2024) reported much larger ejecta mass as compared to the model ejecta masses. K. Maguire et al. (2023) showed that SN 2020udy observations are in good agreement with the `N5def` model, but they also found the slow light-curve evolution of SN 2020udy compared to the `N5def` model. This can be due to more radiation trapping, suggesting deflagration models are underestimating the ejecta mass. Similarly, M. Singh et al. (2022) reported an underestimation of ejecta mass by models for SN 2012Z and SN 2020rea.

M. Singh et al. (2022) reported slow light-curve evolution of SN 2012Z as compared to `N10def` model with ^{56}Ni mass of 0.12 $M_\odot$ and ejecta mass, $M_{\rm ej} = 1.09\ M_\odot$, much higher than the deflagration models. These quantities differ from the model; we scaled the `N10def` model to these parameters, keeping the elemental abundances relative to ^{56}Ni conserved. Also scaling the `N10def` model's density and temperature profile mentioned in Figures 2 and 3, the total dust budget at 4000 days is $1.47 \times 10^{-4}\ M_\odot$. Profiles of each dust species are mentioned in Table 2 and Figure 8.

This result shows that Type Iax ejecta, based on observational constraints, will result in even larger dust masses than those estimated from deflagration models. Further development of theoretical models consistent with observations is required to constrain the results.

7. Comparison with Standard Type Ia Ejecta

As discussed earlier in Section 3, the detonation reduces the important oxidizing agent O but enhances Si abundance, in addition to higher energies leading to lower gas densities. These conditions do not favor dust production in Type Ia SNe. Figure 6 highlights the contribution from different velocity zones in dust production for `N3` model of both deflagration and DDT models. In Type Iax SNe, the higher abundances of IGEs and IMEs in the dense inner regions promote efficient dust production. In contrast, in Type Ia SNe, these elements are pushed outward into lower-density regions, which is less favorable for dust formation. This effect is further

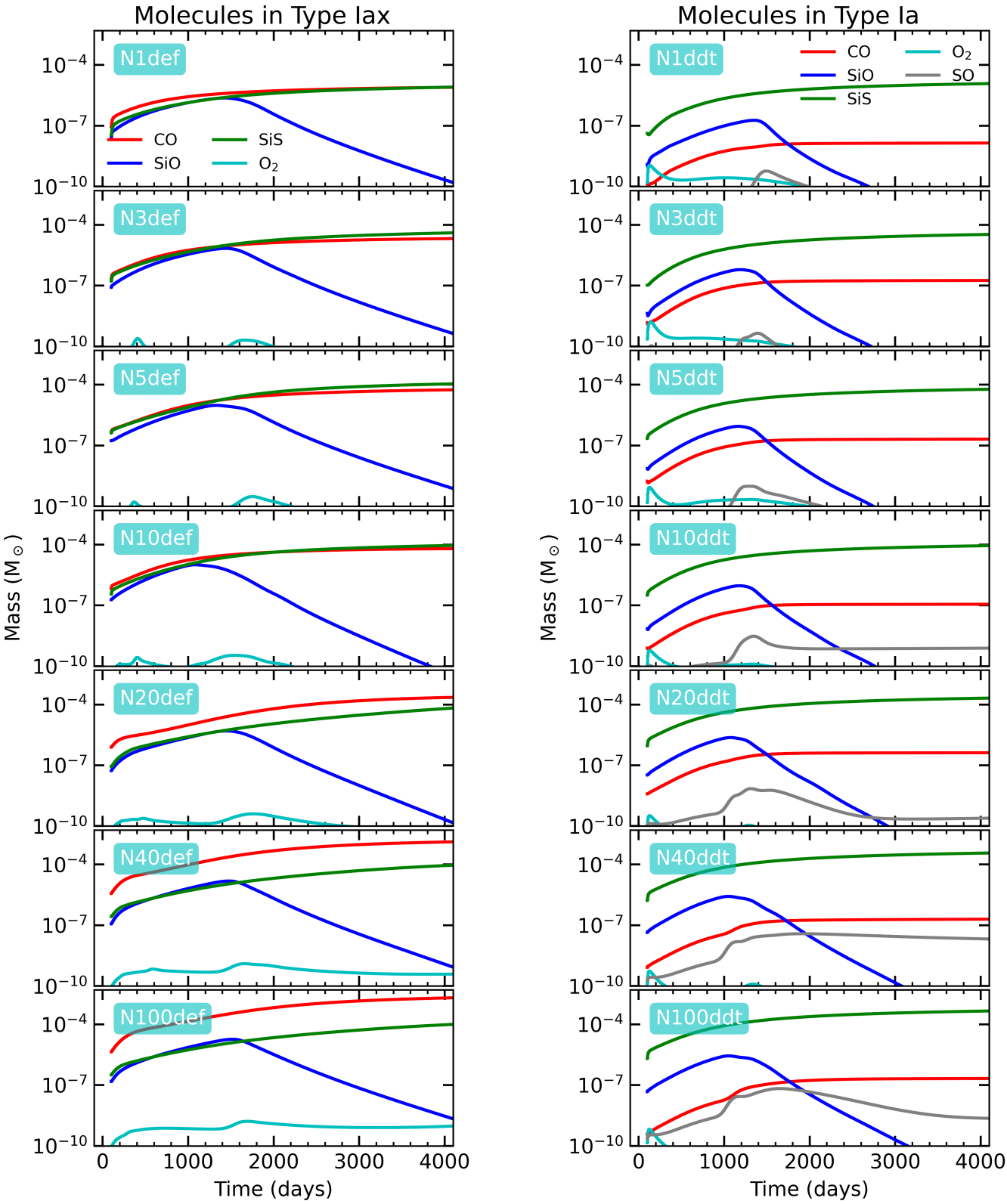

Figure 4. Comparison of molecules produced in Type Iax and Type Ia SN ejecta.

compounded by the CE reactions, since Type Ia produces larger masses of ^{56}Ni.

`N1ddt` model yields dust masses of around 2.7×10^{-7} $M_{\odot}$ at 4000 days. As we go further for higher configuration (`N40ddt, N100ddt`) models, the initial deflagration waves become stronger and give us more mixed layers and less 56Ni content; hence, the dust mass increases. Due to low temperature, the time of dust formation is earlier for Type Iax, but even the `N100ddt` model with high abundances and low ^{56}Ni mass gives a dust mass of around 2.9×10^{-6} $M_{\odot}$ at

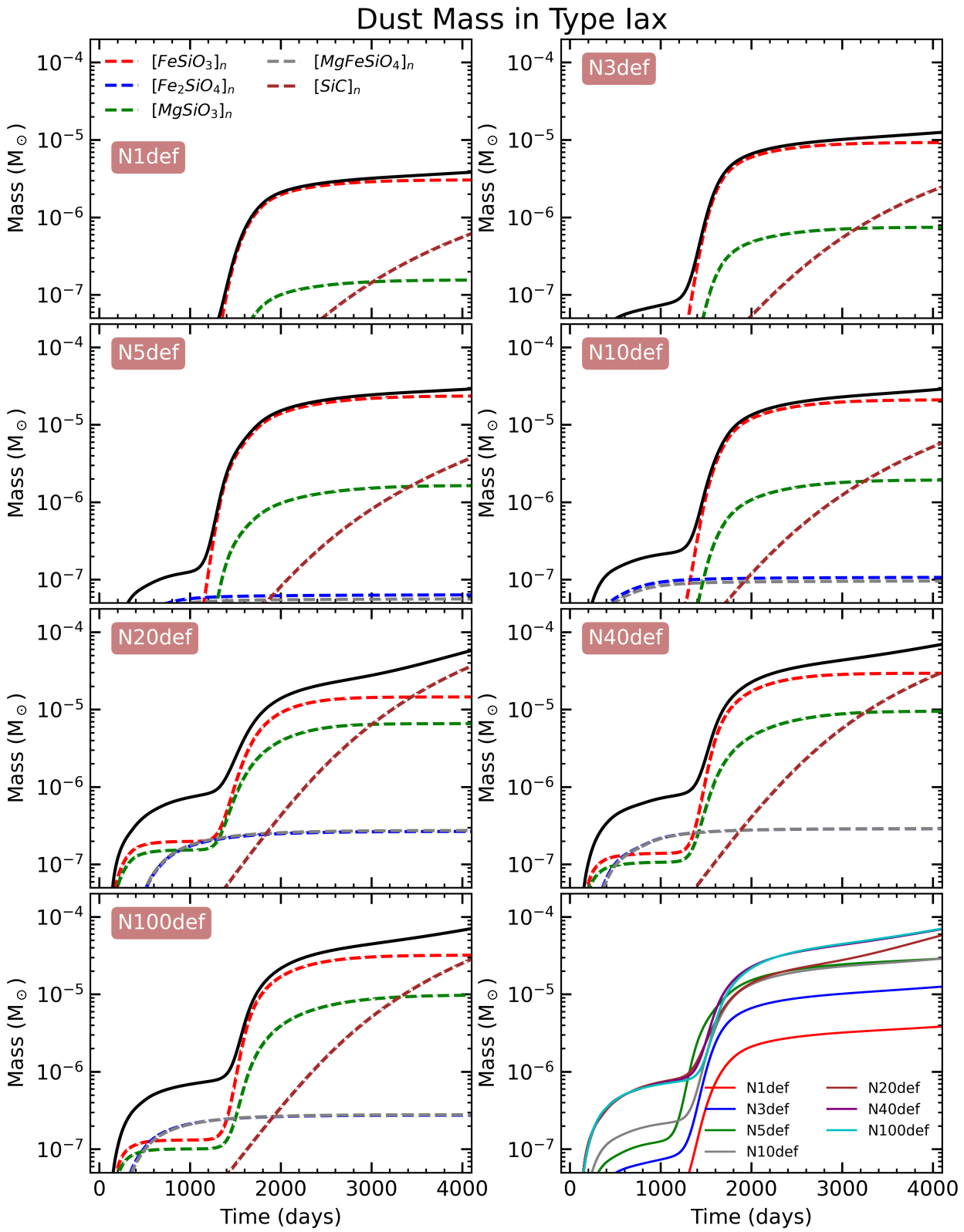

Figure 5. Dust mass evolution in Type Iax SN ejecta for different deflagration models. Each panel shows the time evolution of individual dust species produced in dashed colored lines with the total dust mass in a solid black line. The bottom right panel compares total dust masses across all models.

4000 days, while for other models it ranges from 2.7×10^{-7} $M_\odot$ to 2.7×10^{-6} $M_\odot$, which is far less than the deflagration counterpart. Figure 9 gives us the dust masses produced in all DDT models. Initial models are rich in SiC since Si abundance is higher, and as we go further, ($FeSiO_3$) becomes a significant contributor.

Table 2
Mass Evolution of Individual Dust Species in Time Along with the Total Dust Masses in All Deflagration Models and One Scaled Model for SN 2012Z

Days	$[FeSiO_3]_n$	$[MgSiO_3]_n$	$[Fe_2SiO_4]_n$	$[Mg_2SiO_4]_n$	$[MgFeSiO_4]_n$	$[SiC]_n$	Total Dust Mass
				N1def			
300	2.5×10^{-10}	1.9×10^{-10}	3.2×10^{-9}	1.1×10^{-10}	2.8×10^{-9}	4.3×10^{-11}	6.6×10^{-9}
500	3.4×10^{-10}	2.5×10^{-10}	5.9×10^{-9}	2.1×10^{-10}	5.3×10^{-9}	1.0×10^{-10}	1.2×10^{-8}
800	3.7×10^{-10}	2.8×10^{-10}	8.0×10^{-9}	2.8×10^{-10}	7.1×10^{-9}	3.2×10^{-10}	1.6×10^{-8}
1000	4.7×10^{-10}	2.9×10^{-10}	8.9×10^{-9}	3.1×10^{-10}	7.9×10^{-9}	6.5×10^{-10}	1.9×10^{-8}
1500	3.0×10^{-7}	1.6×10^{-8}	1.0×10^{-8}	3.3×10^{-10}	8.9×10^{-9}	3.6×10^{-9}	3.4×10^{-7}
2000	2.0×10^{-6}	1.0×10^{-7}	1.1×10^{-8}	3.5×10^{-10}	9.3×10^{-9}	1.6×10^{-8}	2.1×10^{-6}
2500	2.6×10^{-6}	1.3×10^{-7}	1.1×10^{-8}	3.5×10^{-10}	9.5×10^{-9}	5.5×10^{-8}	2.8×10^{-6}
3000	2.9×10^{-6}	1.4×10^{-7}	1.1×10^{-8}	3.6×10^{-10}	9.7×10^{-9}	1.4×10^{-7}	3.2×10^{-6}
4000	3.0×10^{-6}	1.5×10^{-7}	1.1×10^{-8}	3.7×10^{-10}	9.9×10^{-9}	5.5×10^{-7}	3.7×10^{-6}
				N3def			
300	2.3×10^{-9}	1.7×10^{-9}	1.2×10^{-8}	6.1×10^{-10}	1.1×10^{-8}	1.3×10^{-10}	2.7×10^{-8}
500	3.0×10^{-9}	2.3×10^{-9}	2.2×10^{-8}	1.1×10^{-9}	2.0×10^{-8}	3.3×10^{-10}	4.9×10^{-8}
800	3.4×10^{-9}	2.6×10^{-9}	3.0×10^{-8}	1.5×10^{-9}	2.7×10^{-8}	1.0×10^{-9}	6.5×10^{-8}
1000	3.6×10^{-9}	2.6×10^{-9}	3.3×10^{-8}	1.7×10^{-9}	3.0×10^{-8}	2.1×10^{-9}	7.3×10^{-8}
1500	8.3×10^{-7}	7.1×10^{-8}	4.0×10^{-8}	1.9×10^{-9}	3.6×10^{-8}	1.2×10^{-8}	9.9×10^{-7}
2000	6.0×10^{-6}	4.8×10^{-7}	4.2×10^{-8}	2.0×10^{-9}	3.8×10^{-8}	5.4×10^{-8}	6.6×10^{-6}
2500	8.0×10^{-6}	6.4×10^{-7}	4.4×10^{-8}	2.1×10^{-9}	4.0×10^{-8}	1.9×10^{-7}	8.9×10^{-6}
3000	8.0×10^{-6}	6.4×10^{-7}	4.4×10^{-8}	2.1×10^{-9}	4.0×10^{-8}	1.9×10^{-7}	1.0×10^{-5}
4000	8.0×10^{-6}	6.4×10^{-7}	4.4×10^{-8}	2.1×10^{-9}	4.0×10^{-8}	1.9×10^{-7}	1.2×10^{-5}
				N5def			
300	5.4×10^{-9}	4.1×10^{-9}	1.9×10^{-8}	6.2×10^{-10}	1.7×10^{-8}	2.1×10^{-10}	4.7×10^{-8}
500	6.6×10^{-9}	5.0×10^{-9}	3.6×10^{-8}	1.2×10^{-9}	3.1×10^{-8}	5.0×10^{-10}	8.1×10^{-8}
800	6.9×10^{-9}	5.3×10^{-9}	5.2×10^{-8}	1.7×10^{-9}	4.6×10^{-8}	1.5×10^{-9}	1.1×10^{-7}
1000	8.7×10^{-9}	5.4×10^{-9}	5.7×10^{-8}	1.9×10^{-9}	5.0×10^{-8}	3.0×10^{-9}	1.3×10^{-7}
1500	3.8×10^{-6}	3.0×10^{-7}	6.1×10^{-8}	2.0×10^{-9}	5.4×10^{-8}	1.7×10^{-8}	4.3×10^{-6}
2000	1.4×10^{-5}	9.7×10^{-7}	6.2×10^{-8}	2.1×10^{-9}	5.5×10^{-8}	8.1×10^{-8}	1.5×10^{-5}
2500	1.9×10^{-5}	1.3×10^{-6}	6.3×10^{-8}	2.1×10^{-9}	5.5×10^{-8}	3.0×10^{-7}	2.1×10^{-5}
3000	2.2×10^{-5}	1.5×10^{-6}	6.3×10^{-8}	2.1×10^{-9}	5.6×10^{-8}	8.1×10^{-7}	2.4×10^{-5}
4000	2.3×10^{-5}	1.6×10^{-6}	6.4×10^{-8}	2.2×10^{-9}	5.6×10^{-8}	3.3×10^{-6}	2.8×10^{-5}
				N10def			
300	1.2×10^{-8}	9.0×10^{-9}	2.7×10^{-8}	1.1×10^{-9}	2.5×10^{-8}	3.1×10^{-10}	7.5×10^{-8}
500	1.4×10^{-8}	1.1×10^{-8}	5.7×10^{-8}	2.5×10^{-9}	5.2×10^{-8}	7.1×10^{-10}	1.4×10^{-7}
800	1.5×10^{-8}	1.2×10^{-8}	8.2×10^{-8}	3.6×10^{-8}	7.4×10^{-8}	2.1×10^{-9}	1.9×10^{-7}
1000	1.5×10^{-8}	1.2×10^{-8}	9.3×10^{-8}	4.0×10^{-8}	8.3×10^{-8}	4.4×10^{-9}	2.1×10^{-7}
1500	1.2×10^{-6}	1.4×10^{-7}	1.0×10^{-7}	4.4×10^{-8}	9.1×10^{-8}	2.5×10^{-8}	1.5×10^{-6}
2000	1.2×10^{-5}	1.0×10^{-6}	1.0×10^{-7}	4.4×10^{-8}	9.4×10^{-8}	1.2×10^{-7}	1.4×10^{-5}
2500	1.7×10^{-5}	1.6×10^{-6}	1.0×10^{-7}	4.5×10^{-8}	9.5×10^{-8}	4.4×10^{-7}	1.9×10^{-5}
3000	1.9×10^{-5}	1.8×10^{-6}	1.1×10^{-7}	4.5×10^{-8}	9.5×10^{-8}	1.2×10^{-6}	2.3×10^{-5}
4000	2.1×10^{-5}	1.9×10^{-6}	1.1×10^{-7}	4.6×10^{-8}	9.6×10^{-8}	5.2×10^{-6}	2.8×10^{-5}
				N20def			
300	1.2×10^{-7}	9.4×10^{-8}	1.8×10^{-9}	5.9×10^{-9}	1.8×10^{-9}	5.1×10^{-10}	2.2×10^{-7}
500	1.8×10^{-7}	1.4×10^{-7}	4.4×10^{-8}	1.8×10^{-8}	4.4×10^{-8}	1.5×10^{-9}	4.2×10^{-7}
800	1.9×10^{-7}	1.5×10^{-7}	1.3×10^{-7}	2.4×10^{-8}	1.3×10^{-7}	5.4×10^{-9}	6.4×10^{-7}
1000	2.0×10^{-7}	1.5×10^{-7}	1.7×10^{-7}	3.3×10^{-8}	1.7×10^{-7}	1.7×10^{-8}	7.3×10^{-7}
1500	1.6×10^{-6}	7.5×10^{-7}	2.3×10^{-7}	3.7×10^{-8}	2.3×10^{-7}	7.5×10^{-8}	2.4×10^{-6}
2000	9.0×10^{-6}	3.9×10^{-6}	2.5×10^{-7}	3.8×10^{-8}	2.6×10^{-7}	4.3×10^{-7}	1.4×10^{-5}
2500	1.3×10^{-5}	5.8×10^{-6}	2.6×10^{-7}	3.8×10^{-8}	2.7×10^{-7}	1.9×10^{-6}	2.2×10^{-5}
3000	1.4×10^{-5}	6.4×10^{-6}	2.6×10^{-7}	3.9×10^{-8}	2.7×10^{-7}	6.3×10^{-6}	2.8×10^{-5}
4000	1.5×10^{-5}	6.6×10^{-6}	2.7×10^{-7}	3.9×10^{-8}	2.8×10^{-7}	3.2×10^{-5}	5.4×10^{-5}
				N40def			
300	9.6×10^{-8}	7.3×10^{-8}	2.7×10^{-8}	1.7×10^{-9}	2.5×10^{-8}	7.1×10^{-10}	2.2×10^{-7}
500	1.3×10^{-7}	9.7×10^{-8}	1.0×10^{-7}	8.9×10^{-9}	9.7×10^{-8}	1.7×10^{-9}	4.3×10^{-7}
800	1.4×10^{-7}	1.1×10^{-7}	1.7×10^{-7}	2.0×10^{-8}	1.7×10^{-7}	5.9×10^{-9}	6.2×10^{-7}
1000	1.4×10^{-7}	1.1×10^{-7}	2.2×10^{-7}	2.6×10^{-8}	2.2×10^{-7}	1.2×10^{-8}	7.2×10^{-7}
1500	1.3×10^{-6}	5.4×10^{-7}	2.6×10^{-7}	3.3×10^{-8}	2.6×10^{-7}	7.5×10^{-8}	2.5×10^{-6}
2000	1.7×10^{-5}	4.5×10^{-6}	2.8×10^{-7}	3.5×10^{-8}	2.8×10^{-7}	4.1×10^{-7}	2.3×10^{-5}

Table 2
(Continued)

Days	$[FeSiO_3]_n$	$[MgSiO_3]_n$	$[Fe_2SiO_4]_n$	$[Mg_2SiO_4]_n$	$[MgFeSiO_4]_n$	$[SiC]_n$	Total Dust Mass
2500	2.5×10^{-5}	7.3×10^{-6}	2.8×10^{-7}	3.7×10^{-8}	2.9×10^{-7}	1.8×10^{-6}	3.5×10^{-5}
3000	2.8×10^{-5}	8.8×10^{-6}	2.8×10^{-7}	3.7×10^{-8}	2.9×10^{-7}	5.7×10^{-6}	4.4×10^{-5}
4000	2.9×10^{-5}	9.4×10^{-6}	2.9×10^{-7}	3.8×10^{-8}	2.9×10^{-7}	2.7×10^{-5}	6.6×10^{-5}
				N100def			
300	9.6×10^{-8}	7.3×10^{-8}	3.2×10^{-8}	1.5×10^{-9}	3.0×10^{-8}	7.1×10^{-10}	2.3×10^{-7}
500	1.2×10^{-7}	9.4×10^{-8}	1.0×10^{-7}	8.6×10^{-9}	9.9×10^{-8}	1.7×10^{-9}	4.2×10^{-7}
800	1.3×10^{-7}	1.0×10^{-7}	1.8×10^{-7}	2.0×10^{-8}	1.8×10^{-7}	5.3×10^{-9}	6.1×10^{-7}
1000	1.3×10^{-7}	1.0×10^{-7}	2.1×10^{-7}	2.5×10^{-8}	2.1×10^{-7}	1.1×10^{-8}	6.9×10^{-7}
1500	7.6×10^{-7}	2.4×10^{-7}	2.5×10^{-7}	3.2×10^{-8}	2.5×10^{-7}	6.4×10^{-8}	1.6×10^{-6}
2000	1.6×10^{-5}	3.9×10^{-6}	2.6×10^{-7}	3.5×10^{-8}	2.6×10^{-7}	3.4×10^{-7}	2.2×10^{-5}
2500	2.7×10^{-5}	7.0×10^{-6}	2.7×10^{-7}	3.6×10^{-8}	2.7×10^{-7}	1.5×10^{-6}	3.6×10^{-5}
3000	3.0×10^{-5}	8.7×10^{-6}	2.7×10^{-7}	3.7×10^{-8}	2.7×10^{-7}	5.1×10^{-6}	4.5×10^{-5}
4000	3.1×10^{-5}	9.7×10^{-6}	2.7×10^{-7}	3.7×10^{-8}	2.8×10^{-7}	2.5×10^{-5}	6.7×10^{-5}
				SN 2012Z			
300	8.67×10^{-8}	6.6×10^{-8}	2.6×10^{-9}	8.5×10^{-10}	3.2×10^{-9}	6.8×10^{-10}	1.6×10^{-7}
500	1.4×10^{-7}	1.1×10^{-7}	9.1×10^{-9}	3.3×10^{-9}	1.2×10^{-8}	1.8×10^{-9}	2.7×10^{-7}
800	1.7×10^{-7}	1.3×10^{-7}	4.8×10^{-8}	1.2×10^{-8}	5.5×10^{-8}	5.0×10^{-9}	4.2×10^{-7}
1000	1.8×10^{-7}	1.4×10^{-7}	7.3×10^{-8}	1.7×10^{-8}	8.3×10^{-8}	9.2×10^{-9}	4.9×10^{-7}
1500	4.9×10^{-6}	3.2×10^{-6}	1.1×10^{-7}	2.5×10^{-8}	1.2×10^{-7}	4.1×10^{-8}	8.3×10^{-6}
2000	3.4×10^{-5}	1.8×10^{-5}	1.2×10^{-7}	2.8×10^{-8}	1.3×10^{-7}	1.7×10^{-7}	5.2×10^{-5}
2500	5.8×10^{-5}	2.9×10^{-5}	1.2×10^{-7}	3.0×10^{-8}	1.4×10^{-7}	6.8×10^{-7}	8.9×10^{-5}
3000	7.3×10^{-5}	3.7×10^{-5}	1.3×10^{-7}	3.1×10^{-8}	1.4×10^{-7}	2.5×10^{-6}	1.1×10^{-4}
4000	8.1×10^{-5}	4.2×10^{-5}	1.3×10^{-7}	3.1×10^{-8}	1.5×10^{-7}	2.3×10^{-5}	1.5×10^{-4}

Note. The masses are in $M_\odot$.

Table 3
Quantitative Comparison of Dust Mass Production in Type Iax SNe (Deflagration) and Type Ia SNe (DDT) Models at 4000 Days

Type Iax			Type Ia		
Def. Model	Dust Mass	Dust/Gas Mass	DDT Model	Dust Mass	Dust/Gas Mass
N1def	3.7×10^{-6}	4.4×10^{-5}	N1ddt	2.7×10^{-7}	1.9×10^{-7}
N3def	1.2×10^{-5}	6.2×10^{-5}	N3ddt	1.6×10^{-6}	1.2×10^{-6}
N5def	2.8×10^{-5}	7.5×10^{-5}	N5ddt	1.7×10^{-6}	1.2×10^{-6}
N10def	2.8×10^{-5}	5.8×10^{-5}	N10ddt	9.9×10^{-7}	7.1×10^{-7}
N20def	5.4×10^{-5}	6.2×10^{-5}	N20ddt	3.3×10^{-6}	2.4×10^{-6}
N40def	6.6×10^{-5}	5.5×10^{-5}	N40ddt	2.7×10^{-6}	1.9×10^{-6}
N100def	6.7×10^{-5}	5.1×10^{-5}	N100ddt	2.9×10^{-6}	2.1×10^{-6}

Note. The dust masses are in $M_\odot$.

Figure 7 highlights the difference between the dust production efficiency of Type Ia and Type Iax SNe. The dust-to-gas mass ratio for Type Iax is about 1 or 2 orders of magnitude larger than the same model of Type Ia, at 4000 days as shown in Table 3. The chemical mixing and incomplete burning due to the pure deflagration are the key factors that make Type Iax SNe potential sources of stellar dust, with a unique abundance of Fe-rich silicates. On the other hand, the models predict a negligible mass of dust to form in standard Type Ia SNe.

8. Implications

C. Pinto et al. (2013), E. Dwek (2016), and I. Psaradaki et al. (2023) found that most of the iron in ISM is depleted from gas, and almost 90% of it is locked in dust. As mentioned earlier, Type II SNe are confirmed dust producers in galaxies, but they form too little Fe and cannot account for iron-rich dust. However, Type Ia SNe are rich in Fe, but there is no observation yet that can confirm dust production in their ejecta. In this case, Type Iax SNe can provide a pathway for iron-rich dust production in SN environments.

Our results highlight the possibility of dust production in Type Iax. Even though the dust masses are only around $5.0 \times 10^{-5}\ M_\odot$, the unique chemical composition in thermonuclear SNe makes this special SN subclass interesting, to study the dust budget. Our results are highly sensitive to ejecta mass and the relative abundances of the elements, ^{56}Ni content, alongside temperatures and density of the environment. As mentioned in Section 6.1, models might underestimate the ejecta mass, and a model scaled to observed parameters gives us higher dust masses.

Our results suggest that silicon carbide dust should form in Type Iax SNe at late times, post 2000 days. In the presolar grains in meteorites, SiC is one of the most commonly found

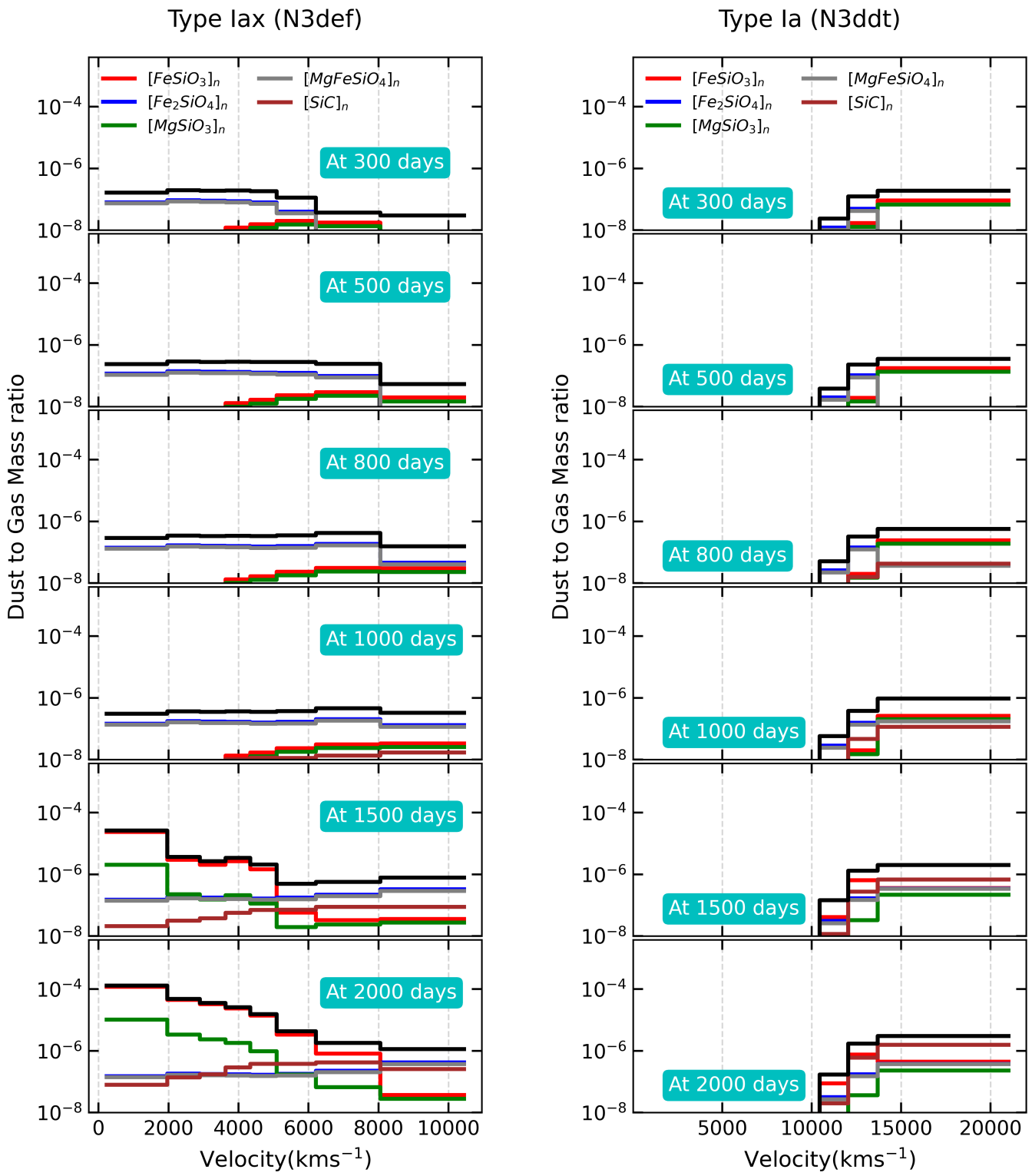

Figure 6. Comparison of dust to gas mass ratio in Type Iax and Type Ia N3 model in velocity coordinate. The plot shows that the N3def model (Type Iax) is much more efficient in dust production than the N3ddt model (Type Ia). The comparison is also highlighting the reason for it, that, in the Type Iax model, the dust formation is more in the inner high-density regions, while, for the Type Ia, dust formation is only possible in the outer low-density regions.

dust species (E. Zinner 2007; L. R. Nittler 2008; P. Hoppe 2010; S. Amari et al. 2013; P. Hoppe et al. 2018, 2019; H. K. Fok et al. 2024; P. Hoppe et al. 2024), attributed to origins in AGB stars as well as core-collapse SNe based on their isotopic ratios. Interestingly, SiC-X grains found in meteorites are reported to have formed in the ejecta at least 2000 day postexplosion in core-collapse SNe (N. Liu et al. 2018; U. Ott et al. 2019). However, in thermonuclear SNe, the abundances of ^{13}C and ^{17}O are very low; those isotopic ratios do not match the reported ratios in presolar grains.

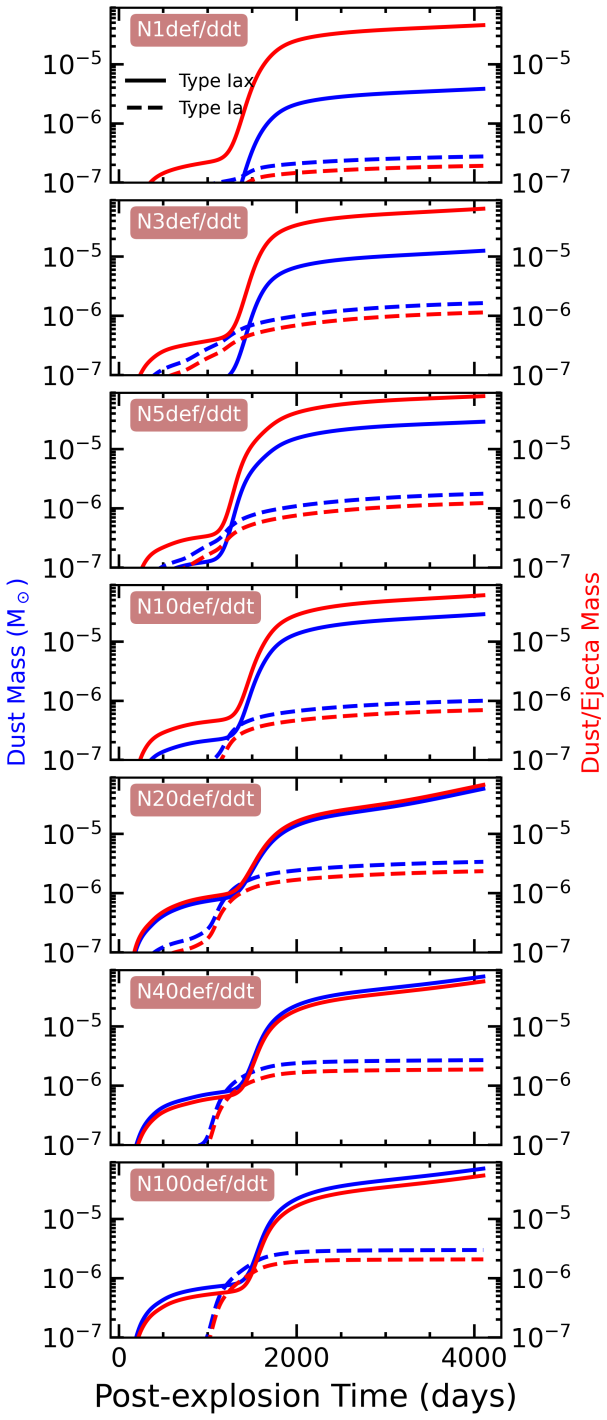

Figure 7. Comparison of dust production efficiency of deflagration and DDT models of similar ignition channels. Solid lines are production outcomes from deflagration (Type Iax) models, and similarly, dashed lines are for DDT (Type Ia) models. The blue lines are for the dust masses produced, and the red lines are for the dust-to-gas mass ratio along postexplosion time.

The model will improve if we have better observational constraints on ejecta mass, dust mass, and gas temperatures. Late-time follow-up observations around 5–6 yr after explosions to look for possible IR emission from dust are required to verify this hypothesis. Since only a small part of the ejecta is involved in dust production, after 4000 days, many elements are still present in gas. They may accrete onto the surfaces of already produced dust grains. We have used a standard prescription of grain growth via accretion (E. Dwek & I. Cherchneff 2011; A. Sarangi et al. 2019), taking μm grains of ($FeSiO_3$) and a sticking coefficient of 0.5 as initial conditions, for both cases of Type Iax (`N3def`) and Type Ia (`N3ddt`) SN ejecta. The results are shown in Figure 10 for possible grain growth up to 1000 yr postexplosion. However, within that period, we did not find any significant change in dust masses due to accretion of metals on the surface.

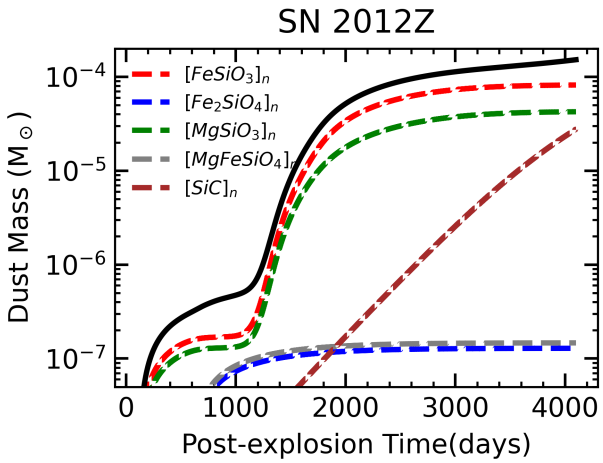

Figure 8. Dust mass evolution of each dust species is shown in dashed lines with total dust mass in a solid black line for the `N10def` model scaled to SN 2012Z ejecta mass.

Spatially resolved galactic SN remnants, such as Pa 30, provide the opportunity to trace the location and composition of dust at late times. Remnant Pa 30 was reported to originate from a subluminous thermonuclear explosion, likely to be a Type Iax SN (T. Cunningham et al. 2024). It is bright in the far-IR wavelengths, revealing the presence of cold dust (F. Lykou et al. 2023). However, the IRAS 12 μm resulted in nondetection. The high-resolution spectrum expected from the ongoing `JWST (GO 9111)` program will enable us to understand the abundance distribution in the nebula, the location of warm dust from its mid-IR emission, and decode whether there is significant dust formation in the ejecta of such SNe.

9. Summary and Conclusion

Our findings suggest that the low-luminosity subclass of Type Ia—the Type Iax SNe— are efficient dust producers. We compare dust production in Type Ia and Type Iax SNe, showing the clear advantage of Type Iax SNe in producing dust in the ejecta. The main highlights for these results are as follows:

1. *Favorable conditions*: The less energetic, pure deflagration explosion in Type Iax SNe leads to several conditions that are ideal for dust formation. The ejecta from Type Iax SNe are slower (2000–7000 km s^{-1}) compared to Type Ia ejecta (10,000–20,000 km s^{-1}). This slower expansion allows the ejecta to maintain a higher density for a longer period. The higher density

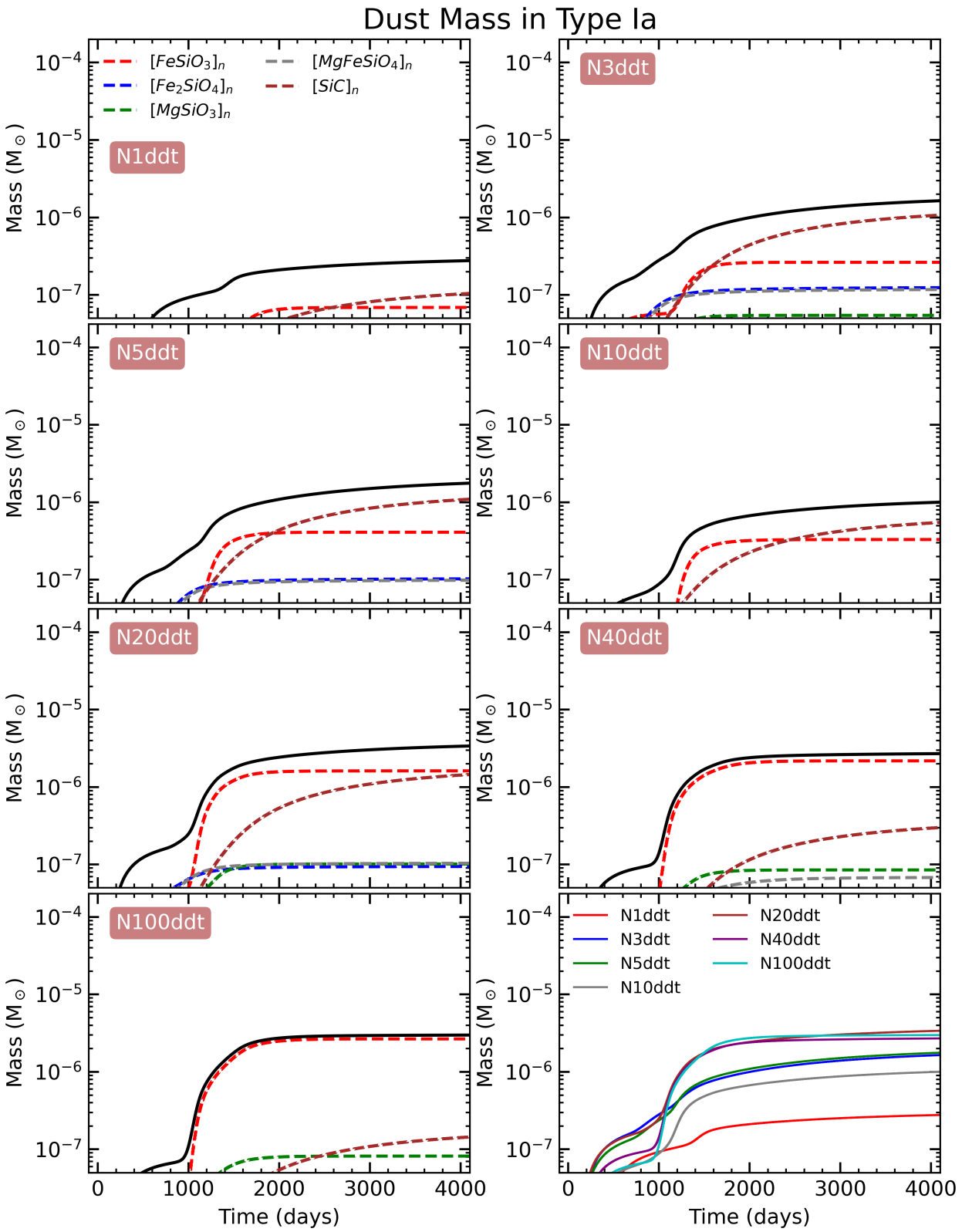

Figure 9. Dust mass evolution in Type Ia SN ejecta for different delayed-detonation models. Each panel shows the time evolution of individual dust species produced in dashed colored lines with the total dust mass in a solid black line. The bottom right panel compares total dust masses across all models (I. R. Seitenzahl et al. 2013).

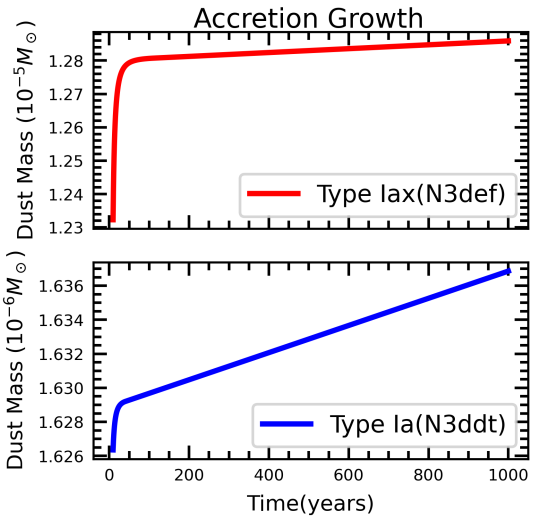

Figure 10. The dust mass growth in Type Iax (`N3def`) and Type Ia (`N3ddt`) ejecta due to accretion on surface of a 0.01 μm ($FeSiO_3$) grain starting from about 7 until 1000 yr.

promotes more frequent collisions between atoms and molecules, which enhances the rate of dust nucleation.

2. *^{56}Ni content*: Type Iax SNe produce significantly less radioactive ^{56}Ni compared to Type Ia SNe. The decay of ^{56}Ni releases high-energy γ-rays, which can destroy newly formed dust and precursor molecules. The lower ^{56}Ni mass in Type Iax SNe allows the ejecta to cool more quickly and reduces this destruction.
3. *Precursor materials*: The incomplete burning in a pure deflagration leaves behind large amounts of unburned carbon (C) and oxygen (O), in addition to IMEs and IGEs. These are the crucial ingredients for forming precursor molecules like CO and SiO, which then lead to the formation of iron-rich dust species such as silicates.
4. *Dust masses*: At 4000 days after the explosion, the dust mass produced by Type Iax SNe models ranged from 3.7×10^{-6} to 6.7×10^{-5} $M_\odot$. In contrast, Type Ia SNe models produced much less dust, ranging from 2.7×10^{-7} to 2.9×10^{-6} $M_\odot$. The dust-to-gas mass ratio, a measure of production efficiency, was also much higher for Type Iax SNe, at about 4 to 8×10^{-5}, while, for Type Ia SNe, it was only about 0.2–2.4×10^{-6}. A model scaled to reported ejecta mass of SN 2012Z produces a dust mass of 1.5×10^{-4} $M_\odot$ and dust-to-gas mass ratio of 1.4×10^{-4} much more efficient than the `N100ddt` model consistent with Type Ia ejecta.
5. *State-of-the-art model*: Our model accounts for a comprehensive nonequilibrium chemical evolution of Type Ia SNe. The small to negligible dust masses we predict are in agreement with nondetections of dust emission in a typical Type Ia SN ejecta (H. L. Gomez et al. 2012). We propose that, due to the use of classical nucleation theory, the previous model of Type Ia SNe by T. Nozawa et al. (2011) largely overestimates the dust masses.
6. *Chemical network*: The chemical pathway that leads to the synthesis of Fe-rich silicates in SNe is developed in this study, and can be used for any other stellar or SN environments. This result in a larger context can shed some light on how iron is integrated in dust grains, and so is depleted from the ISM (E. Dwek 2016).

Acknowledgments

The authors gratefully acknowledge the support of the Department of Science and Technology (DST), and the Council of Scientific & Industrial Research (CSIR), Government of India. We also extend our sincere thanks to Dr. Barnabas Barna, Dr. Mridweeka Singh, Prof. Saurabh Jha, Prof. D. K. Sahu, and Mr. Hrishav Das for very insightful discussions.

Appendix

In Tables A1 and A2, we present the nuclear reaction network adopted in this work, along with the Compton Electron-induced Reactions of ^{56}Ni used in our calculations.

Table A1
New Chemical Network Added to Current Analysis

Reaction	Reactants		Products	A_{ij}	ν	E_a	References
			(Fe_nO_m) cluster				
1	$Fe+O_2$	$\rightarrow$	$FeO+O$	2.0900×10^{-9}	0.0	10,199.6	NIST
2	$FeO+O$	$\rightarrow$	$Fe+O_2$	4.6000×10^{-10}	−0.4	350.0	""
3	$Fe+CO_2$	$\rightarrow$	$FeO+CO$	5.3800×10^{-10}	0.0	15,033.1	""
4	$Fe+O_2$	$\rightarrow$	FeO_2	2.0500×10^{-28}	−2.6	3170.2	""
5	$FeO+O_2$	$\rightarrow$	FeO_2+O	1.0200×10^{-11}	0.4	8202.8	""
6	$FeO+CO_2$	$\rightarrow$	FeO_2+CO	6.4800×10^{-9}	0.0	22,979.5	""
7	$FeO+FeO_2$	$\rightarrow$	Fe_2O_3	1.0000×10^{-11}	0.0	500.0	E
8	FeO_2+FeO_2	$\rightarrow$	Fe_2O_3+O	1.0000×10^{-11}	0.0	500.0	""
9	$FeO+FeO$	$\rightarrow$	Fe_2O_2	4.6086×10^{-17}	0.0	−2821.4	SC13-SiO
10	Fe_2O_2+FeO	$\rightarrow$	Fe_3O_3	2.2388×10^{-15}	0.0	−2878.9	""
11	$Fe_2O_2+Fe_2O_2$	$\rightarrow$	Fe_3O_3+FeO	1.5265×10^{-14}	0.0	−2386.8	""
12	Fe_2O_2	$\rightarrow$	$FeO+FeO$	7.7200×10^{-7}	0.0	0.0	""
13	Fe_3O_3	$\rightarrow$	Fe_2O_2+FeO	7.8300×10^{-6}	0.0	0.0	""
14	$Fe_2O_2+O_2$	$\rightarrow$	Fe_2O_3+O	1.0000×10^{-11}	0.0	500.0	""
15	Fe_2O_2+SO	$\rightarrow$	Fe_2O_3+S	1.0000×10^{-11}	0.0	500.0	""
16	Fe_2O_3+O	$\rightarrow$	$Fe_2O_2+O_2$	1.0000×10^{-12}	0.0	0.0	""
17	Fe_2O_3+S	$\rightarrow$	Fe_2O_2+SO	1.0000×10^{-12}	0.0	0.0	""
18	$Fe_3O_3+O_2$	$\rightarrow$	Fe_3O_4+O	1.0000×10^{-13}	0.0	500.0	""

Table A1
(Continued)

Reaction	Reactants		Products	A_{ij}	ν	E_a	References
19	Fe_3O_3+SO	→	Fe_3O_4+S	1.0000×10^{-13}	0.0	500.0	“”
20	Fe_2O_3+FeO	→	Fe_3O_4	7.4626×10^{-16}	0.0	−2878.9	“”
21	Fe_2O_2+FeO	→	Fe_2O_3+Fe	7.4626×10^{-16}	0.0	−2878.9	“”
22	Fe_3O_3+FeO	→	Fe_3O_4+Fe	5.0884×10^{-15}	0.0	−2386.8	“”
23	Fe+Fe_2O_3	→	Fe_2O_2+FeO	1.0000×10^{-15}	0.0	4000.0	“”
24	Fe+Fe_3O_4	→	Fe_3O_3+FeO	1.0000×10^{-15}	0.0	8000.0	“”
			$[Mg_{1-x}Fe_xSiO_3]$ and $[Mg_{1-x}Fe_xSiO_4]$ clusters				
25	Mg+Si_2O_3	→	$MgSi_2O_3$	1.0000×10^{-12}	0.0	0.0	SC13
26	$MgSi_2O_3$+O_2	→	$MgSi_2O_4$+O	1.0000×10^{-12}	0.0	0.0	“”
27	$MgSi_2O_4$+Mg	→	$Mg_2Si_2O_4$	1.0000×10^{-12}	0.0	0.0	“”
28	$Mg_2Si_2O_4$+O_2	→	$Mg_2Si_2O_5$+O	1.0000×10^{-12}	0.0	0.0	“”
29	$Mg_2Si_2O_5$+O_2	→	$Mg_2Si_2O_6$+O	1.0000×10^{-12}	0.0	0.0	“”
30	$Mg_2Si_2O_6$+Mg	→	$Mg_3Si_2O_6$	1.0000×10^{-12}	0.0	0.0	“”
31	$Mg_3Si_2O_6$+O_2	→	$Mg_3Si_2O_7$+O	1.0000×10^{-12}	0.0	0.0	“”
32	$Mg_3Si_2O_7$+Mg	→	$Mg_4Si_2O_7$	1.0000×10^{-12}	0.0	0.0	“”
33	$Mg_4Si_2O_7$+O_2	→	$Mg_4Si_2O_8$+O	1.0000×10^{-12}	0.0	0.0	“”
34	$MgSi_2O_3$+SO	→	$MgSi_2O_4$+S	1.0000×10^{-12}	0.0	0.0	“”
35	$Mg_2Si_2O_4$+SO	→	$Mg_2Si_2O_5$+S	1.0000×10^{-12}	0.0	0.0	“”
36	$Mg_2Si_2O_5$+SO	→	$Mg_2Si_2O_6$+S	1.0000×10^{-12}	0.0	0.0	“”
37	$Mg_3Si_2O_6$+SO	→	$Mg_3Si_2O_7$+S	1.0000×10^{-12}	0.0	0.0	“”
38	$Mg_4Si_2O_7$+SO	→	$Mg_4Si_2O_8$+S	1.0000×10^{-12}	0.0	0.0	“”
39	Fe+Si_2O_3	→	$FeSi_2O_3$	1.0000×10^{-12}	0.0	0.0	as 25
40	$FeSi_2O_3$+O_2	→	$FeSi_2O_4$+O	1.0000×10^{-12}	0.0	0.0	as 26
41	$FeSi_2O_4$+Fe	→	$Fe_2Si_2O_4$	1.0000×10^{-12}	0.0	0.0	as 27
42	$Fe_2Si_2O_4$+O_2	→	$Fe_2Si_2O_5$+O	1.0000×10^{-12}	0.0	0.0	as 28
43	$Fe_2Si_2O_5$+O_2	→	$Fe_2Si_2O_6$+O	1.0000×10^{-12}	0.0	0.0	as 29
44	$Fe_2Si_2O_6$+Fe	→	$Fe_3Si_2O_6$	1.0000×10^{-12}	0.0	0.0	as 30
45	$Fe_3Si_2O_6$+O_2	→	$Fe_3Si_2O_7$+O	1.0000×10^{-12}	0.0	0.0	as 31
46	$Fe_3Si_2O_7$+Fe	→	$Fe_4Si_2O_7$	1.0000×10^{-12}	0.0	0.0	as 32
47	$Fe_4Si_2O_7$+O_2	→	$Fe_4Si_2O_8$+O	1.0000×10^{-12}	0.0	0.0	as 33
48	$FeSi_2O_3$+SO	→	$FeSi_2O_4$+S	1.0000×10^{-12}	0.0	0.0	as 34
49	$Fe_2Si_2O_4$+SO	→	$Fe_2Si_2O_5$+S	1.0000×10^{-12}	0.0	0.0	as 35
50	$Fe_2Si_2O_5$+SO	→	$Fe_2Si_2O_6$+S	1.0000×10^{-12}	0.0	0.0	as 36
51	$Fe_3Si_2O_6$+SO	→	$Fe_3Si_2O_7$+S	1.0000×10^{-12}	0.0	0.0	as 37
52	$Fe_4Si_2O_7$+SO	→	$Fe_4Si_2O_8$+S	1.0000×10^{-12}	0.0	0.0	as 38
53	$MgSi_2O_4$+Fe	→	$MgFeSi_2O_4$	1.0000×10^{-12}	0.0	0.0	as 27
54	$FeSi_2O_4$+Mg	→	$MgFeSi_2O_4$	1.0000×10^{-12}	0.0	0.0	“”
55	$MgFeSi_2O_4$+O_2	→	$MgFeSi_2O_5$+O	1.0000×10^{-12}	0.0	0.0	as 28
56	$MgFeSi_2O_5$+O_2	→	$MgFeSi_2O_6$+O	1.0000×10^{-12}	0.0	0.0	as 29
57	$Fe_2Si_2O_6$+Mg	→	$MgFe_2Si_2O_6$	1.0000×10^{-12}	0.0	0.0	as 29
58	$MgFeSi_2O_6$+Mg	→	$Mg_2FeSi_2O_6$	1.0000×10^{-12}	0.0	0.0	as 30
59	$MgFeSi_2O_6$+Fe	→	$MgFe_2Si_2O_6$	1.0000×10^{-12}	0.0	0.0	“”
60	$MgFe_2Si_2O_6$+O_2	→	$MgFe_2Si_2O_7$+O	1.0000×10^{-12}	0.0	0.0	as 31
61	$Mg_2FeSi_2O_6$+O_2	→	$Mg_2FeSi_2O_7$+O	1.0000×10^{-12}	0.0	0.0	“”
62	$Fe_3Si_2O_7$+Mg	→	$MgFe_3Si_2O_7$	1.0000×10^{-12}	0.0	0.0	as 32
63	$MgFe_2Si_2O_7$+Mg	→	$Mg_2Fe_2Si_2O_7$	1.0000×10^{-12}	0.0	0.0	“”
64	$MgFe_2Si_2O_7$+Fe	→	$MgFe_3Si_2O_7$	1.0000×10^{-12}	0.0	0.0	“”
65	$Mg_2FeSi_2O_7$+Mg	→	$Mg_3FeSi_2O_7$	1.0000×10^{-12}	0.0	0.0	“”
66	$Mg_2FeSi_2O_7$+Fe	→	$Mg_2Fe_2Si_2O_7$	1.0000×10^{-12}	0.0	0.0	“”
67	$MgFe_3Si_2O_7$+O_2	→	$MgFe_3Si_2O_8$+O	1.0000×10^{-12}	0.0	0.0	as 33
68	$Mg_2Fe_2Si_2O_7$+O_2	→	$Mg_2Fe_2Si_2O_8$+O	1.0000×10^{-12}	0.0	0.0	“”
69	$Mg_3FeSi_2O_7$+O_2	→	$Mg_3FeSi_2O_8$+O	1.0000×10^{-12}	0.0	0.0	as 34
70	$MgFeSi_2O_4$+SO	→	$MgFeSi_2O_5$+S	1.0000×10^{-12}	0.0	0.0	as 35
71	$MgFeSi_2O_5$+SO	→	$MgFeSi_2O_6$+S	1.0000×10^{-12}	0.0	0.0	as 36
72	$MgFe_2Si_2O_6$+SO	→	$MgFe_2Si_2O_7$+S	1.0000×10^{-12}	0.0	0.0	as 37
73	$Mg_2FeSi_2O_6$+SO	→	$Mg_2FeSi_2O_7$+S	1.0000×10^{-12}	0.0	0.0	“”
74	$MgFe_3Si_2O_7$+SO	→	$MgFe_3Si_2O_8$+S	1.0000×10^{-12}	0.0	0.0	as 38
75	$Mg_2Fe_2Si_2O_7$+SO	→	$Mg_2Fe_2Si_2O_8$+S	1.0000×10^{-12}	0.0	0.0	“”
76	$Mg_3FeSi_2O_7$+SO	→	$Mg_3FeSi_2O_8$+S	1.0000×10^{-12}	0.0	0.0	“”
77	$FeSi_2O_3$+O	→	($FeSiO_3$)+SiO	1.0000×10^{-12}	0.0	0.0	E
78	$Fe_2Si_2O_4$+O	→	(Fe_2SiO_4)+SiO	1.0000×10^{-12}	0.0	0.0	“”
79	$MgFeSi_2O_4$+O	→	($MgFeSiO_4$)+SiO	1.0000×10^{-12}	0.0	0.0	“”

Table A1
(Continued)

Reaction	Reactants		Products	A_{ij}	ν	E_a	References
80	$MgSi_2O_3$+O	→	$(MgSiO_3)$+SiO	1.0000×10^{-12}	0.0	0.0	""
81	$Mg_2Si_2O_4$+O	→	Mg_2SiO_4+SiO	1.0000×10^{-12}	0.0	0.0	""
			Cluster fragmentation				
82	FeO+M	→	Fe+O+M	4.4000×10^{-10}	0.0	98,600.0	E
83	Fe_2O_2+M	→	FeO+FeO+M	4.4000×10^{-10}	0.0	98,600.0	as 82
84	FeO_2+M	→	FeO+O+M	8.0180×10^{-11}	0.0	26,900.0	SC13-SiO
85	Fe_2O_3+M	→	Fe_2O_2+O+M	5.0000×10^{-10}	0.0	55,000.0	""
86	Fe_3O_3+M	→	Fe_2O_2+FeO+M	4.4000×10^{-10}	0.0	98,600.0	""
87	Fe_3O_4+M	→	Fe_3O_3+O+M	5.0000×10^{-10}	0.0	55,000.0	""
88	$MgSi_2O_3$+M	→	Si_2O_3+Mg+M	1.0000×10^{-10}	0.0	98,600.0	""
89	$MgSi_2O_3$+M	→	$(MgSiO_3)$+Si+M	1.0000×10^{-10}	0.0	98,600.0	E
90	$Mg_2Si_2O_4$+M	→	Mg_2SiO_4+Si+M	1.0000×10^{-10}	0.0	98,600.0	""
91	$MgSi_2O_4$+M	→	$MgSi_2O_3$+O+M	1.0000×10^{-10}	0.0	98,600.0	SC13
92	$Mg_2Si_2O_4$+M	→	$MgSi_2O_4$+Mg+M	1.0000×10^{-10}	0.0	98,600.0	""
93	$Mg_2Si_2O_5$+M	→	$Mg_2Si_2O_4$+O+M	1.0000×10^{-10}	0.0	98,600.0	""
94	$Mg_2Si_2O_6$+M	→	$Mg_2Si_2O_5$+O+M	1.0000×10^{-10}	0.0	98,600.0	""
95	$Mg_3Si_2O_6$+M	→	$Mg_2Si_2O_6$+Mg+M	1.0000×10^{-10}	0.0	98,600.0	""
96	$Mg_3Si_2O_7$+M	→	$Mg_3Si_2O_6$+O+M	1.0000×10^{-10}	0.0	98,600.0	""
97	$Mg_4Si_2O_7$+M	→	$Mg_3Si_2O_7$+Mg+M	1.0000×10^{-10}	0.0	98,600.0	""
98	$Mg_4Si_2O_8$+M	→	$Mg_4Si_2O_7$+O+M	1.0000×10^{-10}	0.0	98,600.0	""
99	$FeSi_2O_3$+M	→	Si_2O_3+Fe+M	1.0000×10^{-10}	0.0	98,600.0	as 88
100	$FeSi_2O_3$+M	→	$(FeSiO_3)$+SiO+M	1.0000×10^{-10}	0.0	98,600.0	as 89
101	$Fe_2Si_2O_4$+M	→	(Fe_2SiO_4)+SiO+M	1.0000×10^{-10}	0.0	98,600.0	as 90
102	$FeSi_2O_4$+M	→	$FeSi_2O_3$+O+M	1.0000×10^{-10}	0.0	98,600.0	as 91
103	$Fe_2Si_2O_4$+M	→	$FeSi_2O_4$+Fe+M	1.0000×10^{-10}	0.0	98,600.0	as 92
104	$Fe_2Si_2O_5$+M	→	$Fe_2Si_2O_4$+O+M	1.0000×10^{-10}	0.0	98,600.0	as 93
105	$Fe_2Si_2O_6$+M	→	$Fe_2Si_2O_5$+O+M	1.0000×10^{-10}	0.0	98,600.0	as 94
106	$Fe_3Si_2O_6$+M	→	$Fe_2Si_2O_6$+Fe+M	1.0000×10^{-10}	0.0	98,600.0	as 95
107	$Fe_3Si_2O_7$+M	→	$Fe_3Si_2O_6$+O+M	1.0000×10^{-10}	0.0	98,600.0	as 96
108	$Fe_4Si_2O_7$+M	→	$Fe_3Si_2O_7$+Fe+M	1.0000×10^{-10}	0.0	98,600.0	as 97
109	$Fe_4Si_2O_8$+M	→	$Fe_4Si_2O_7$+O+M	1.0000×10^{-10}	0.0	98,600.0	as 98
110	$MgFeSi_2O_4$+M	→	$FeSi_2O_4$+Mg+M	1.0000×10^{-10}	0.0	98,600.0	as 90
111	$MgFeSi_2O_4$+M	→	$MgSi_2O_4$+Fe+M	1.0000×10^{-10}	0.0	98,600.0	""
112	$MgFeSi_2O_4$+M	→	$(MgFeSiO_4)$+Si+M	1.0000×10^{-10}	0.0	98,600.0	""
113	$MgFeSi_2O_5$+M	→	$MgFeSi_2O_4$+O+M	1.0000×10^{-10}	0.0	98,600.0	as 93
114	$MgFeSi_2O_6$+M	→	$MgFeSi_2O_5$+O+M	1.0000×10^{-10}	0.0	98,600.0	as 94
115	$MgFe_2Si_2O_6$+M	→	$Fe_2Si_2O_6$+Mg+M	1.0000×10^{-10}	0.0	98,600.0	as 95
116	$MgFe_2Si_2O_6$+M	→	$MgFeSi_2O_6$+Fe+M	1.0000×10^{-10}	0.0	98,600.0	""
117	$Mg_2FeSi_2O_6$+M	→	$MgFeSi_2O_6$+Mg+M	1.0000×10^{-10}	0.0	98,600.0	""
118	$Mg_2FeSi_2O_6$+M	→	$Mg_2Si_2O_6$+Fe+M	1.0000×10^{-10}	0.0	98,600.0	""
119	$MgFe_2Si_2O_7$+M	→	$MgFe_2Si_2O_6$+O+M	1.0000×10^{-10}	0.0	98,600.0	as 96
120	$Mg_2FeSi_2O_7$+M	→	$Mg_2FeSi_2O_6$+O+M	1.0000×10^{-10}	0.0	98,600.0	""
121	$MgFe_3Si_2O_7$+M	→	$Fe_3Si_2O_7$+Mg+M	1.0000×10^{-10}	0.0	98,600.0	as 97
122	$MgFe_3Si_2O_7$+M	→	$MgFe_2Si_2O_7$+Fe+M	1.0000×10^{-10}	0.0	98,600.0	""
123	$Mg_2Fe_2Si_2O_7$+M	→	$MgFe_2Si_2O_7$+Mg+M	1.0000×10^{-10}	0.0	98,600.0	""
124	$Mg_2Fe_2Si_2O_7$+M	→	$Mg_2FeSi_2O_7$+Fe+M	1.0000×10^{-10}	0.0	98,600.0	""
125	$Mg_3FeSi_2O_7$+M	→	$Mg_2FeSi_2O_7$+Mg+M	1.0000×10^{-10}	0.0	98,600.0	""
126	$Mg_3FeSi_2O_7$+M	→	$Mg_3Si_2O_7$+Fe+M	1.0000×10^{-10}	0.0	98,600.0	""
127	$MgFe_3Si_2O_8$+M	→	$MgFe_3Si_2O_7$+O+M	1.0000×10^{-10}	0.0	98,600.0	as 98
128	$Mg_2Fe_2Si_2O_8$+M	→	$Mg_2Fe_2Si_2O_7$+O+M	1.0000×10^{-10}	0.0	98,600.0	""
129	$Mg_3FeSi_2O_8$+M	→	$Mg_3FeSi_2O_7$+O+M	1.0000×10^{-10}	0.0	98,600.0	""
130	$(MgSiO_3)$+M	→	MgO_2+SiO+M	1.0000×10^{-10}	0.0	98,600.0	E
131	Mg_2SiO_4+M	→	$(MgSiO_3)$+MgO+M	1.0000×10^{-10}	0.0	98,600.0	
132	$(FeSiO_3)$+M	→	FeO_2+SiO+M	1.0000×10^{-10}	0.0	98,600.0	""
133	(Fe_2SiO_4)+M	→	$(FeSiO_3)$+FeO+M	1.0000×10^{-10}	0.0	98,600.0	""
134	$(MgFeSiO_4)$+M	→	$(FeSiO_3)$+MgO+M	1.0000×10^{-10}	0.0	98,600.0	""
135	$(MgFeSiO_4)$+M	→	$(MgSiO_3)$+FeO+M	1.0000×10^{-10}	0.0	98,600.0	""

Note. The rates mentioned are calculated using Chemical Kinetic approach (either theoretical, experimental from database or estimated from similar reactions). The reaction rates are expressed in Arrhenius form $k = A_{ij} \times (T/300K)^{\nu} \times \exp(-E_a/T)$ with A_{ij} in s^{-1}, $cm^3\ s^{-1}$, or $cm^6\ s^{-1}$ for unimolecular, bimolecular, and termolecular processes, respectively; E_a is in Kelvin. SC13: A. Sarangi & I. Cherchneff (2013); SC13-SiO: similar to SiO network in A. Sarangi & I. Cherchneff (2013); NIST: NIST/Kinetics; E: estimated.

Table A2
Compton Electron-induced Reactions, Corresponding Mean Energy per Ion Pair W_i from A. Sarangi & I. Cherchneff (2013), and Arrhenius Coefficient A as a Function of Ejecta Model

Species	Reactions	W_i(eV)	N1def $^{56}Ni = 0.034 M_\odot$ A- 0.08 $M_\odot^a$	N10def $^{56}Ni = 0.183 M_\odot$ A- 0.48 $M_\odot^b$	N100def $^{56}Ni = 0.355 M_\odot$ A- 1.31 $M_\odot^c$	N100ddt $^{56}Ni = 0.604 M_\odot$ A- 1.4 $M_\odot^d$
CO	$\rightarrow O^+ + C$	768	2.33×10^{-8}	1.58×10^{-7}	1.94×10^{-7}	1.73×10^{-7}
	$\rightarrow O + C^+$	247	7.25×10^{-8}	4.92×10^{-7}	6.05×10^{-7}	5.37×10^{-7}
	$\rightarrow C + O$	125	1.43×10^{-7}	9.72×10^{-7}	1.19×10^{-6}	1.06×10^{-6}
	$\rightarrow CO^+ + e^-$	34	5.27×10^{-7}	3.57×10^{-6}	4.39×10^{-6}	3.90×10^{-6}
O	$\rightarrow O^+ + e^-$	46.2	3.88×10^{-7}	2.63×10^{-6}	3.23×10^{-6}	2.87×10^{-6}
C	$\rightarrow C^+ + e^-$	36.4	4.92×10^{-7}	3.34×10^{-6}	4.10×10^{-6}	3.64×10^{-6}
SiO	$\rightarrow O^+ + Si$	678	2.64×10^{-8}	1.79×10^{-7}	2.20×10^{-7}	1.96×10^{-7}
	$\rightarrow O + Si^+$	218	8.21×10^{-8}	5.57×10^{-7}	6.85×10^{-7}	6.08×10^{-7}
	$\rightarrow O + Si$	110	1.63×10^{-7}	1.10×10^{-6}	1.36×10^{-6}	1.21×10^{-6}
	$\rightarrow SiO^+ + e^-$	30	5.97×10^{-6}	4.05×10^{-6}	4.98×10^{-6}	4.42×10^{-6}
Ne	$\rightarrow Ne^+ + e^-$	36.4	4.92×10^{-7}	3.34×10^{-6}	4.10×10^{-6}	3.64×10^{-6}

Note. The rates are expressed in an Arrhenius form. See I. Cherchneff & E. Dwek (2009) for details. k_C^a: $A \times (T/T_0)^{0.43} \exp(-2324.88/T)$ k_C^b: $A \times (T/T_0)^{0.08} \exp(-2082.99/T)$ k_C^c: $A \times (T/T_0)^{0.11} \exp(-1335.44/T)$ k_C^d: $A \times (T/T_0)^{0.06} \exp(-1259.58/T)$.

ORCID iDs

Aman Kumar https://orcid.org/0009-0004-0041-9271
Arkaprabha Sarangi https://orcid.org/0000-0002-9820-679X

References

Amari, S., Zinner, E., & Gallino, R. 2014, AIPC, 1594, 307
Arnett, W. D. 1982, ApJ, 253, 785
Bánhidi, D., Barna, B., Szalai, T., et al. 2025, A&A, 703, A64
Barna, B., Szalai, T., Jha, S. W., et al. 2021, MNRAS, 501, 1078
Barna, B., Szalai, T., Kerzendorf, W. E., et al. 2018, MNRAS, 480, 3609
Bersten, M. C., & Mazzali, P. A. 2017, in in Handbook of Supernovae, ed. A. W. Alsabti & P. Murdin (Springer), 723
Branch, D., Baron, E., Thomas, R. C., et al. 2004, PASP, 116, 903
Camacho-Neves, Y., Jha, S. W., Barna, B., et al. 2023, ApJ, 951, 67
Cherchneff, I., & Dwek, E. 2009, ApJ, 703, 642
Cherchneff, I., & Dwek, E. 2010, ApJ, 713, 1
Clayton, G. C., Wesson, R., Fox, O. D., et al. 2025, ApJ, 991, 133
Colgate, S. A., & McKee, C. 1969, ApJ, 157, 623
Cunningham, T., Caiazzo, I., Prusinski, N. Z., et al. 2024, ApJL, 975, L7
Dimitriadis, G., Burgaz, U., Deckers, M., et al. 2025, A&A, 694, A10
Donn, B., & Nuth, J. A. 1985, ApJ, 288, 187
Dwek, E. 2016, ApJ, 825, 136
Dwek, E., & Cherchneff, I. 2011, ApJ, 727, 63
Elias, J., Frogel, J. A., Hackwell, J., & Persson, S. 1981, ApJL, 251, L13
Fink, M., Kromer, M., Seitenzahl, I. R., et al. 2014, MNRAS, 438, 1762
Fok, H. K., Pignatari, M., Côté, B., & Trappitsch, R. 2024, ApJL, 977, L24
Foley, R. J., Challis, P. J., Chornock, R., et al. 2013, ApJ, 767, 57
Foley, R. J., Jha, S. W., Pan, Y.-C., et al. 2016, MNRAS, 461, 433
Foley, R. J., McCully, C., Jha, S. W., et al. 2014, ApJ, 792, 29
Fox, O. D., Johansson, J., Kasliwal, M., et al. 2016, ApJL, 816, L13
Gamezo, V. N., Khokhlov, A. M., Oran, E. S., Chtchelkanova, A. Y., & Rosenberg, R. O. 2003, Sci, 299, 77
García-Senz, D., & Bravo, E. 2005, A&A, 430, 585
Gomez, H. L., Clark, C. J. R., Nozawa, T., et al. 2012, MNRAS, 420, 3557
Hillebrandt, W., Kromer, M., Röpke, F. K., & Ruiter, A. J. 2013, FrPhy, 8, 116
Hoeflich, P., Khokhlov, A. M., & Wheeler, J. C. 1995, ApJ, 444, 831
Hoppe, P. 2010, in Nuclei in the Cosmos, 21
Hoppe, P., Leitner, J., Pignatari, M., & Amari, S. 2024, MNRAS, 532, 211
Hoppe, P., Pignatari, M., Kodolányi, J., Gröner, E., & Amari, S. 2018, GeCoA, 221, 182
Hoppe, P., Stancliffe, R. J., Pignatari, M., & Amari, S. 2019, ApJ, 887, 8
Hoyle, F., & Fowler, W. A. 1960, ApJ, 132, 565
Jack, D., Hauschildt, P. H., & Baron, E. 2011, A&A, 528, A141
Jha, S. W. 2017, Type Iax Supernovae (Springer), 375
Jha, S. W., Maguire, K., & Sullivan, M. 2019, NatAs, 3, 706
Jordan, G. C., IV, Perets, H. B., Fisher, R. T., & van Rossum, D. R. 2012, ApJL, 761, L23
Kasen, D. 2006, ApJ, 649, 939
Kawabata, M., Kawabata, K. S., Maeda, K., et al. 2018, PASJ, 70, 111
Kawabata, M., Maeda, K., Yamanaka, M., et al. 2021, PASJ, 73, 1295
Kwok, L. A., Singh, M., Jha, S. W., et al. 2025, ApJL, 989, L33
Lach, F., Callan, F. P., Bubeck, D., et al. 2022, A&A, 658, A179
Li, L., Wang, X., Zhang, J., et al. 2018, MNRAS, 478, 4575
Li, W., Filippenko, A. V., Chornock, R., et al. 2003, PASP, 115, 453
Li, W., Filippenko, A. V., Treffers, R. R., et al. 2001, ApJ, 546, 734
Liu, N., Nittler, L. R., Alexander, C. M. O. D., & Wang, J. 2018, SciA, 4, eaao1054
Liu, Z.-W., Röpke, F. K., & Han, Z. 2023, RAA, 23, 082001
Liu, Z.-W., Stancliffe, R. J., Abate, C., & Wang, B. 2015, ApJ, 808, 138
Long, M., Jordan, G. C., IV, van Rossum, D. R., et al. 2014, ApJ, 789, 103
Lykou, F., Parker, Q. A., Ritter, A., et al. 2023, ApJ, 944, 120
Ma, H., Woosley, S. E., Malone, C. M., Almgren, A., & Bell, J. 2013, ApJ, 771, 58
Magee, M. R., Killestein, T. L., Pursiainen, M., et al. 2025, MNRAS, 543, 3731
Magee, M. R., Kotak, R., Sim, S. A., et al. 2016, A&A, 589, A89
Maguire, K., Magee, M. R., Leloudas, G., et al. 2023, MNRAS, 525, 1210
Matsuura, M., Dwek, E., Barlow, M. J., et al. 2015, ApJ, 800, 50
Nittler, L. R. 2008, in Nuclei in the Cosmos (NIC X) ads
Nomoto, K., Thielemann, F.-K., & Yokoi, K. 1984, ApJ, 286, 644
Nozawa, T., Maeda, K., Kozasa, T., et al. 2011, ApJ, 736, 45
Ott, U., Stephan, T., Hoppe, P., & Savina, M. R. 2019, ApJ, 885, 128
Pinto, C., Kaastra, J. S., Costantini, E., & de Vries, C. 2013, A&A, 551, A25
Psaradaki, I., Costantini, E., Rogantini, D., et al. 2023, A&A, 670, A30
Rodríguez, Ó., Maoz, D., & Nakar, E. 2023, ApJ, 955, 71
Röpke, F. K., Gieseler, M., Reinecke, M., Travaglio, C., & Hillebrandt, W. 2006, A&A, 453, 203
Röpke, F. K., & Niemeyer, J. C. 2007, A&A, 464, 683
Röpke, F. K., Woosley, S. E., & Hillebrandt, W. 2007, ApJ, 660, 1344
Sarangi, A. 2022, A&A, 668 (2022) A57, 10.1051/0004-6361/202244391
Sarangi, A., & Cherchneff, I. 2013, ApJ, 776, 107
Sarangi, A., & Cherchneff, I. 2015, A&A, 575, A95
Sarangi, A., Dwek, E., & Kazanas, D. 2019, ApJ, 885, 126
Sarangi, A., Matsuura, M., & Micelotta, E. R. 2018, SSRv, 214, 63
Seitenzahl, I. R., Ciaraldi-Schoolmann, F., Röpke, F. K., et al. 2013, MNRAS, 429, 1156
Seitenzahl, I. R., Timmes, F. X., & Magkotsios, G. 2014, ApJ, 792, 10
Shahbandeh, M., Sarangi, A., Temim, T., et al. 2023, MNRAS, 523, 6048
Singh, M., Kwok, L. A., Jha, S. W., et al. 2025, arXiv:2505.02943

Singh, M., Misra, K., Sahu, D. K., et al. 2018, MNRAS, 474, 2551
Singh, M., Misra, K., Sahu, D. K., et al. 2022, MNRAS, 517, 5617
Singh, M., Sahu, D. K., Barna, B., et al. 2024, ApJ, 965, 73
Srivastav, S., Smartt, S. J., Huber, M. E., et al. 2023, ApJL, 943, L20
Stritzinger, M., Mazzali, P. A., Sollerman, J., & Benetti, S. 2006, A&A, 460, 793
Thielemann, F.-K., Nomoto, K., & Yokoi, K. 1986, A&A, 158, 17
Wang, L., Hu, M., Wang, L., et al. 2024, NatAs, 8, 504
Woosley, S. E., Taam, R. E., & Weaver, T. A. 1986, ApJ, 301, 601
Zhang, M., Fuller, J., Schwab, J., & Foley, R. J. 2019, ApJ, 872, 29
Zhou, P., Leung, S.-C., Li, Z., et al. 2021, ApJ, 908, 31
Zinner, E. 2007, Treatise on Geochemistry (Pergamon)